

# A variational level set methodology without reinitialization for the prediction of equilibrium interfaces over arbitrary solid surfaces

Karim Alame<sup>a</sup>, Sreevatsa Anantharamu<sup>a</sup>, Krishnan Mahesh<sup>a,\*</sup>

<sup>a</sup>Department of Aerospace Engineering and Mechanics, University of Minnesota, Minneapolis, MN 55455, USA

## ARTICLE INFO

### Article history:

Received 30 June 2018

Received in final form 10 September 2018

Accepted 13 January 2019

Available online 15 May 2019

Communicated by S. Sarkar

2000 MSC: 41A05, 41A10, 65D05, 65D17

**Keywords:** variational level set, level set method, DRLSE, multiphase, reinitialization, distance regularization, Gibbs free energy, roughness

## ABSTRACT

A robust numerical methodology to predict equilibrium interfaces over arbitrary solid surfaces is developed. The kernel of the proposed method is the distance regularized level set equations (DRLSE) with techniques to incorporate the no-penetration and mass-conservation constraints. In this framework, we avoid reinitialization typically used in traditional level set methods. This allows for a more efficient algorithm since only one advection equation is solved, and avoids numerical error associated with the re-distancing step. A novel surface tension distribution, based on harmonic mean, is prescribed such that the zero level set has the correct the liquid-solid surface tension value. This leads to a more accurate triple contact point location. The method uses second-order central difference schemes which facilitates easy parallel implementation, and is validated by comparing to traditional level set methods for canonical problems. The application of the method, in the context of Gibbs free energy minimization, to obtain liquid-air interfaces is validated against existing analytical solutions. The capability of our current methodology to predict equilibrium shapes over both structured and realistic rough surfaces is demonstrated.

© 2022 Elsevier Inc. All rights reserved.

## 1. Introduction

Traditional level set (LS) formulation of moving fronts, as devised by Osher and Sethian (1988), has been used for a wide variety of problems (Malladi et al., 1994; Sethian, 1999; Osher and Fedkiw, 2006). This is due to its relative ease of implementation, simplicity in applying Boolean operations, and ability to handle surface pinching or merging without the need for direct user intervention or complicated algorithms that detect when to perform ‘surgery’. Implementing the traditional level set methods (LSM) requires the use of upwind schemes to maintain numerical stability. As the LS evolves with time, the values of level set function (LSF) begin to drift away from the original

\*Corresponding author: Tel.: +1-612-624-4175; Email: [kmahesh@umn.edu](mailto:kmahesh@umn.edu);

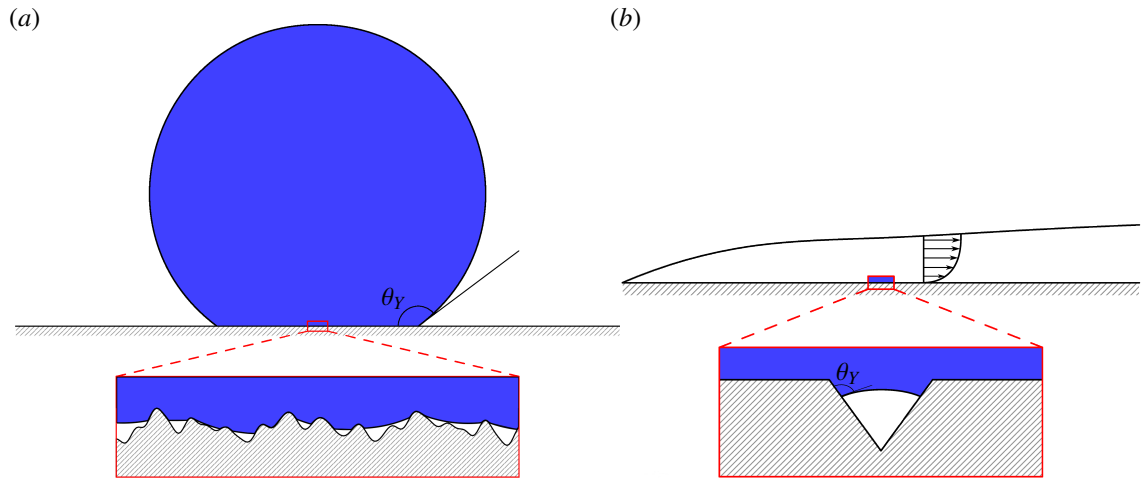


Fig. 1: (a) A schematic of a liquid droplet on a solid substrate and a zoomed in view of the liquid-solid contact showing air pockets where the surface roughness is more apparent. (b) a schematic of a boundary layer with a zoom in view depicting an vapor pocket that grows due to a pressure gradient across a surface cavity. Young's contact angle is given by  $\theta_y$ .

signed distance function (SDF), the LSF often become steep or flat near the zero LS which affects stability. One way to remedy this is to re-initialize the LS equation to restore the LSF back to a SDF. This process is also problem dependent; the reinitialization needs to be done occasionally if the approximation of the LS is not sensitive to its approximation of a SDF. Otherwise, the reinitialization needs to be done every iteration which can get computationally expensive. The first reinitialization method was proposed by Chopp (1993) which directly computes the SDF. The process was computationally expensive and was restricted to a band of points near the zero LS front. This lead to difficulties to locate and discretize the front. The method proposed by Sussman et al. (1994) solves the reinitialization equation iteratively but fails when the LSF is far from a SDF. Peng et al. (1999) proposed a model that addresses the previous issue; however, numerical error tends to shift the interface slightly (Osher and Fedkiw, 2006).

In the context of variational LS formulations, Li et al. (2010) proposed a energy functional that regularizes the distance function as the LS deviates from a SDF. This is known as the distance regularized level set evolution (DRLSE) where the regularization term acts as a penalty to the deviation, thus maintaining a SDF without the need for an explicit reinitialization step. This was employed in the context of image segmentation but was not extended to solve general level set evolution (LSE) equations. The variational LSM without reinitialization have advantages over traditional LSM which include ease of implementation and higher efficiency due to lower computational cost and the ability to use finite difference schemes instead of upwind schemes. Therefore, it is clear that LSE equations can be categorized into a PDE-based LSM (derived from motion equations) and variational LSM (derived via minimizing a certain energy functional) both of which can lead to similar governing equations while keeping the final steady state solution the same.

The main goal of this paper is to devise an easy, fast, accurate and robust method for calculating the equilibrium position of a liquid meniscus over an arbitrary rough surface. Having a model to predict equilibrium position of an interface and its failure criterion is of great importance to numerical simulations and experiments. Figure 1(a)

shows a schematic of a liquid droplet sitting on a solid substrate with a close-up of the surface and (b) a trapped vapor bubble growing out of a cavity due to a pressure gradient present in the boundary layer. Note that the problem can be broken into a macroscopic and a microscopic one. A macroscopic problem relies on predicting the liquid drop shape at equilibrium while conserving its mass. A microscopic problem deals with finding the equilibrium position of the meniscus on a rough substrate given an external pressure. A robust super-hydrophobic surface should be designed to make a stable Cassie state and increase the critical pressure. In the context of cavitation, predicting nucleation sites and the critical pressure that causes vapor pockets to expand beyond the envelope of the cavity into the liquid is of great importance, where the presence of a hydrophobic surface would cause heterogeneous nucleation sites (Brennen, 2014). Carbone and Mangialardi (2005) introduced an analytical model for a simple cosine substrate and then a numerical model to predict interface shape over a two-dimensional (2D) rough periodic substrate defined by a fractal dimension (Bottiglione and Carbone, 2012). Extension to higher dimensions was not explored. Chen et al. (2005) explored the effect of anisotropy of roughness on wetting using Surface Evolver (Brakke, 1992). The Surface Evolver is three-dimensional (3D) but relies on triangulating the interfacial surface. This may require special attention during pinching and breakup. Also, the rough substrate was modeled as a simple grooved channel; it is not clear whether a more complicated geometry can be incorporated. Zhao et al. (1998) used the traditional LSM to capture the behavior of bubbles drops on a macroscopic scale, details of the interface shape and contact angles were not compared quantitatively to existing analytical solutions but their qualitative results were encouraging. In our model, a variational level set methodology without reinitialization is used to capitalize on its advantages introduced earlier. The regularization term is based on the algorithm proposed by Li et al. (2010) which was only applied in the context of image segmentation to the best of our knowledge. We show that the DRLSE can be used in the context of both PDE-based and variational derived LSM. The algorithm minimizes the Gibbs free energy which is written in a general form that allows for the control of the dissolved gas saturation levels. The results show that the proposed model is effective in handling complicated geometries and is able to accurately predict interfacial equilibrium positions.

The paper is organized as follows: the level set formulation, terminology and notation, in both the traditional and variational sense, is presented in §2. A general framework for the Gibbs free energy equation, based on Xiang et al. (2017), written in the variational LS framework is introduced in §3; it allows for prescribing an external pressure and dissolved gas saturation levels. The algorithm and numerical implementation is presented in §4. It is validated with canonical level set test cases (e.g. curvature driven flow and motion in the normal direction) in §5. This is crucial since minimizing the LSF of the Gibbs free energy leads to a governing evolution equation that can be written as a combination of motion in the normal direction with curvature driven diffusion. The Gibbs energy model is validated with the analytic solution of the Young-Laplace equation and the solution over a cosine substrate derived by Carbone and Mangialardi (2005). Results of our numerical experiments, to highlight the robustness of the code, are shown in §6. The numerical experiments explore the equilibrium shape of a drop/interface over a variety of rough substrates that include longitudinal grooves, posts and realistically rough surfaces. Finally, the paper is summarized in §7.

## 2. Level Set Formulation

### 2.1. Traditional Level Set Formulation

Traditional level set formulation of moving fronts introduces an implicit level set function  $\phi(\mathbf{x}, t)$  such that the zero level set contour represents the required interface  $\Gamma = \{\mathbf{x} | \phi(\mathbf{x}, t) = 0\}$ . Given the interface  $\Gamma(t)$  bounding an open region  $\Omega^+$ , we wish to compute its evolution under a velocity field  $\mathbf{u}(\mathbf{x}, t)$ . This velocity can be a function of the interfacial geometry (e.g. normals or curvature), position, time, or external physics. The level set function  $\phi$  has the following properties:

$$\phi(\mathbf{x}, t) > 0 \text{ for } \mathbf{x} \in \Omega^+ \quad (1)$$

$$\phi(\mathbf{x}, t) = 0 \text{ for } \mathbf{x} \in \partial\Omega \quad (2)$$

$$\phi(\mathbf{x}, t) < 0 \text{ for } \mathbf{x} \in \Omega^- , \quad (3)$$

where  $\Omega^+$  is the interior of the region bounded by  $\Gamma$ ,  $\partial\Omega := \Gamma$ , and  $\Omega^-$  the exterior region of  $\Gamma$  given by its complement of  $\Omega^+ \cup \partial\Omega$ . The normal to any level set is given by

$$\mathbf{N} = \frac{\nabla\phi(\mathbf{x}, t)}{|\nabla\phi(\mathbf{x}, t)|}, \quad (4)$$

and the corresponding curvature of the interface is given by the divergence of its normal defined as:

$$\kappa = \nabla \cdot \left( \frac{\nabla\phi(\mathbf{x}, t)}{|\nabla\phi(\mathbf{x}, t)|} \right). \quad (5)$$

The area (volume in 3D) of the domain enclosed by  $\Omega$ :

$$\text{area}(\Omega) = \int_{\Omega} H(\phi(\mathbf{x}, t)) \, d\mathbf{x}, \quad (6)$$

where  $H(\phi(\mathbf{x}, t))$  is the Heaviside function

$$H(\phi(\mathbf{x}, t)) = \begin{cases} 1 & \text{if } \phi(\mathbf{x}, t) \geq 0, \\ 0 & \text{if } \phi(\mathbf{x}, t) < 0. \end{cases} \quad (7)$$

The directional derivative of  $H(\phi(\mathbf{x}, t))$  in the normal direction  $\mathbf{N}$  is given by the Dirac delta function:

$$\hat{\delta}(\mathbf{x}, t) = \nabla H(\phi(\mathbf{x}, t)) \cdot \mathbf{N} \quad (8)$$

such that it is non-zero on  $\partial\Omega$  where  $\phi(\mathbf{x}, t) = 0$ . This can be rewritten as

$$\hat{\delta}(\mathbf{x}, t) = H'(\phi(\mathbf{x}, t))\nabla\phi(\mathbf{x}, t) \cdot \mathbf{N} = H'(\phi(\mathbf{x}, t))|\nabla\phi(\mathbf{x}, t)|, \quad (9)$$

where the one-dimensional delta function is defined as  $\delta(\phi(\mathbf{x}, t)) = H'(\phi(\mathbf{x}, t))$  in a distribution sense. The length (surface area in 3D) of an interface  $\Gamma(t)$  can therefore be directly found using the surface integral:

$$\text{length}(\Gamma) = \int_{\Omega} \delta(\phi(\mathbf{x}, t))|\nabla\phi(\mathbf{x}, t)| \, d\mathbf{x}. \quad (10)$$

The motion of the interface is analyzed by convecting all the values of the level set function  $\phi(\mathbf{x}, t)$  with the velocity  $\mathbf{u}(\mathbf{x}, t)$  according to a general equation of motion given by:

$$\frac{\partial \phi}{\partial t} + \mathbf{u} \cdot \nabla \phi = \kappa |\nabla \phi|, \quad (11)$$

where the right-hand side determines the rate of diffusion. The above equation can be expressed in operator form as:

$$\frac{\partial \phi}{\partial t} = L[\phi], \quad (12)$$

where  $L[\phi]$  is the operator approximating all of the right hand side of the equation.

### 2.1.1. Re-initializing Signed Distance Functions

As the level set  $\phi(\mathbf{x}, t)$  evolves with time, the values of  $\phi(\mathbf{x}, t)$  begin to drift away from the original signed distance function (SDF). The level sets deteriorate to form shocks, flat or steep shapes. One way to remedy this is to re-initialize the level set equation to restore  $\phi(\mathbf{x}, t)$  back to a SDF. Sussman et al. (1994) proposed the reinitialization equation given by:

$$\frac{\partial \phi}{\partial t} + S(\phi_o)(|\nabla \phi| - 1) = 0, \quad (13)$$

where  $S(\phi_o)$  is a sign function that is 1 in  $\Omega^+$ , 0 on  $\partial\Omega$  and  $-1$  on  $\Omega^-$ . However, this may cause a circular dependency since the values near the interface in  $\Omega^+$  use  $\phi(\mathbf{x}, t)$  in  $\Omega^-$  for the boundary points and vice versa. This balances out if we assume that  $\phi$  remains smooth at all times, which is not always the case. If  $\phi$  is not smooth or steeper on one side, then the circular dependency may lead the reinitialization equation to move the interface to an incorrect location. Therefore, a numerically smeared out sign function is typically used instead:

$$S(\phi_o) = \frac{\phi_o}{\sqrt{\phi_o^2 + (\Delta x)^2}}, \quad (14)$$

where  $S(\phi_o)$  remains constant for the duration on reinitialization, and has better properties if  $\phi(\mathbf{x}, t)$  is not smooth or if  $|\nabla \phi_o|$  is far from 1. The numerical smearing also reduces its magnitude, causing a slower propagation speed of the information near the interface thereby reducing circular dependencies. In an ideal case, the interface remains stationary during reinitialization. However, numerical error tends to shift the interface slightly (Osher and Fedkiw, 2006). In summary, reinitialization still comes at a computational cost and the inconsistency between theory and implementation remains.

## 2.2. Variational Level Set Formulation

An alternative to the evolution of a PDE-based LSM can be directly derived from the problem of minimizing a certain energy functional defined by the level set function. This is known as the variational level set method (Zhao et al., 1998). The variational formulation is proposed as follows, let an energy functional  $\mathcal{J}(\phi)$  be defined as:

$$\mathcal{J}(\phi) = \mathcal{E}_{int}(\phi) + \mathcal{E}_{ext}(\phi), \quad (15)$$

where  $\mathcal{E}_{ext}(\phi)$  is the external energy functional related to a physical mechanism to be determined, and  $\mathcal{E}_{int}(\phi)$  is the internal energy functional given by:

$$\mathcal{E}_{int}(\phi) = \alpha \mathcal{R}_p(\phi), \quad (16)$$

where  $\alpha$  is positive parameter that controls the effect of  $\mathcal{R}_p(\phi)$  which penalizes the deviation of  $\phi(\mathbf{x}, t)$  from a SDF. To minimize the energy functional  $\mathcal{J}(\phi)$ , we need to find the steady state solution of  $\phi(\mathbf{x}, t)$  by stepping in the direction of steepest descent of  $\mathcal{J}(\phi)$  given by its negative Fréchet derivative  $\mathcal{J}'(\phi)$  such that

$$\phi^{n+1} = \phi^n - \gamma \mathcal{J}'(\phi^n), \quad (17)$$

where  $\gamma$  is the step size taken to be as a ‘time-step’  $\delta t$ . We can write the evolution equation as a gradient flow that minimizes  $\mathcal{J}(\phi)$ :

$$\frac{\partial \phi}{\partial t} = -\frac{\partial \mathcal{J}}{\partial \phi}, \quad (18)$$

where this can also be expressed as Eq. (12):

$$\frac{\partial \phi}{\partial t} = L[\phi]. \quad (19)$$

The above equation highlights the fact that we can obtain the same operator for the traditional and variational formulation of the level set methodology. The key difference is how this operator is discretized and solved; this will be discussed later in §4.

### 2.2.1. Distance regularization as an alternative to reinitialization

It is crucial to keep the level set as an approximate SDF during its evolution as discussed in 2.1.1, where any function  $\phi(\mathbf{x}, t)$  satisfying  $|\nabla \phi| = 1$  is a SDF (Arnold, 2012). Li et al. (2010) proposed a energy functional that regularizes the distance function as the level set deviates from a SDF in the vicinity of the front. This is known as the distance regularized level set evolution (DRLSE) where the penalty functional is given by:

$$\mathcal{R}_p(\phi) = \int_{\Omega} p(|\nabla \phi|) \, dx; \quad (20)$$

this serves as a metric to characterize how close is  $\phi(\mathbf{x}, t)$  to a SDF. The energy density  $p$  is a potential function defined as:

$$p(|\nabla \phi|) = \begin{cases} \frac{1}{(2\pi)^2} (1 - \cos(2\pi|\nabla \phi|)) & \text{if } |\nabla \phi| < 1, \\ \frac{1}{2} (|\nabla \phi| - 1)^2 & \text{if } |\nabla \phi| \geq 1. \end{cases} \quad (21)$$

It is evident that  $p(|\nabla \phi|)$  has two minimums at  $|\nabla \phi| = 0$  and  $|\nabla \phi| = 1$ . The function  $p(|\nabla \phi|)$  is twice differentiable, this can be verified by finding the roots of its first derivative and checking the sign of the second derivative,  $p'(|\nabla \phi|)$  and  $p''(|\nabla \phi|)$  respectively, such that

$$p'(|\nabla \phi|) = \begin{cases} \frac{1}{2\pi} \sin(2\pi|\nabla \phi|) & \text{if } |\nabla \phi| < 1, \\ |\nabla \phi| - 1 & \text{if } |\nabla \phi| \geq 1 \end{cases} \quad (22)$$

and

$$p''(|\nabla \phi|) = \begin{cases} \cos(2\pi|\nabla \phi|) & \text{if } |\nabla \phi| < 1, \\ 1 & \text{if } |\nabla \phi| \geq 1. \end{cases} \quad (23)$$

The roots of  $p'(|\nabla\phi|)$  are seen at the zero line intersection for  $|\nabla\phi| = 0, 0.5$  and  $1$ . The sign of  $p''(|\nabla\phi|)$ , which is positive for  $|\nabla\phi| = 0$  and  $1$ , indicates that they are minimums. The Fréchet derivative in the  $L^2$  inner product of the regularization energy functional  $\mathcal{R}_p(\phi)$  can be shown to be:

$$\frac{\partial \mathcal{R}_p}{\partial \phi} = -\nabla \cdot (d_p(|\nabla\phi|)\nabla\phi), \quad (24)$$

where  $d_p$  is defined as

$$d_p(|\nabla\phi|) = p'(|\nabla\phi|)/|\nabla\phi|. \quad (25)$$

The use of a double-well potential has more favorable properties than using a simple potential function  $\frac{1}{2}(|\nabla\phi| - 1)^2$  which was initially introduced in Li et al. (2005). The advantage is seen in the limiting values of  $|\nabla\phi|$  given by

$$\lim_{|\nabla\phi| \rightarrow 0} d_p(|\nabla\phi|) = \lim_{|\nabla\phi| \rightarrow \infty} d_p(|\nabla\phi|) = 1. \quad (26)$$

We can verify that the boundedness is lost for the simple potential function which can lead to undesirable effects

$$\lim_{|\nabla\phi| \rightarrow 0} |d_p(|\nabla\phi|)| = \infty. \quad (27)$$

Physically, in the regions where  $|\nabla\phi|$  is close to zero, the diffusion rate is positive and arbitrarily large. For this case, the diffusion is backwards, which drastically increases  $|\nabla\phi|$  causing oscillations to appear as peaks and valleys in the final level set  $\phi$ . The oscillations appear at a distance from the zero crossing of the level set but nevertheless may cause a slight shift in the interface location. Therefore for a double-well potential, the function  $d_p(|\nabla\phi|)$  is always bounded such that

$$|d_p(|\nabla\phi|)| < 1, \text{ for all values of } |\nabla\phi| \in [0, \infty). \quad (28)$$

For  $0 < |\nabla\phi| < 1/2$ , the diffusion rate  $d_p(|\nabla\phi|)$  is positive, resulting in a forward diffusion which further decreases  $|\nabla\phi|$  to zero. For  $(1/2) < |\nabla\phi| < 1$ , the diffusion rate  $d_p(|\nabla\phi|)$  is negative, resulting in a backward diffusion which increases  $|\nabla\phi|$  towards unity. For  $|\nabla\phi| > 1$ , the diffusion is positive again which leads to a backward diffusing, reducing the value of  $|\nabla\phi|$  towards 1.

### 3. The model: Gibbs free energy

Consider a thermodynamic system in its general form comprised of a surface, submerged in a bulk liquid consisting of water and dissolved gas, and entrapped air bubbles within the surface cavities consisting of vapor and free gas. The equilibrium liquid-gas interface position is obtained through the minimization of the total Gibbs free energy of a multi-component system (Landau and Lifshitz, 1980; Patankar, 2009) that is given by:

$$G_{tot} = \sum_{\iota} (U_{\iota} + p_L V_{\iota} - T S_{\iota}) + G_{int}, \quad (29)$$

where  $G_{tot}$  denotes the total Gibbs free energy,  $U_{\iota}$  the internal energy of the system,  $p_L$  the liquid pressure,  $V_{\iota}$  the volume of each phase  $\iota$  in the system,  $T$  the temperature, and  $S_{\iota}$  the entropy of the each phase.  $G_{int}$  denotes the free energy of all interfaces present in the system,

$$G_{int} = \sum_{\iota} (\tau_{LG} A_{LG}^{\iota} + \tau_{SG} A_{SG}^{\iota}) + \tau_{LS} A_{LS}, \quad (30)$$

where  $\tau_{LG}$ ,  $\tau_{SG}$  and  $\tau_{LS}$  represent the surface tension of the liquid-gas (LG), solid-gas (SG) and liquid-solid (LS) interfaces respectively. Similarly  $A_{LS}$ ,  $A_{SG}$  and  $A_{LG}$  represent the surface areas of each corresponding phase. It can be shown that using a thermodynamic analysis, the total free energy can be written in a form shown by Xiang et al. (2017),

$$G_{tot} = (p_L - p_G - p_V)V_G + \tau_{LG}(A_{LG} + A_{SG} \cos \theta_Y) + n_G RT \ln \frac{p_G}{s(p_L - p_V^*)} + n_V RT \ln \frac{p_V}{p_V^*} + G_o(p_L, T, s). \quad (31)$$

Here, the first term in the right-hand side of Eq. (31) is attributed to the bulk phases, where  $p_G$  and  $p_V$  are the entrapped gas and vapor pressure respectively, and  $V_G$  the volume of the entrapped gas. The second term represents surface tension attributed to the interface simplified using Young's equation, where  $\theta_Y$  is Young's contact angle. The third term is attributed to the difference in chemical potential between the free gas in the entrapped air within the cavity and dissolved gas in the liquid phase where  $n_G$  is the mole number of entrapped gas,  $R$  the ideal gas constant,  $T$  the temperature,  $s$  the dissolved gas saturation level and  $p_V^*$  the saturated vapor pressure. The fourth term is the energy contribution of unsaturated vapor where  $n_V$  is the mole number of vapor in the cavity. The last term  $G_o$  is the free energy of the Wenzel state which is a constant for a given  $p_L$ ,  $T$ , and  $s$  at the reference state where,

$$G_o(p_L, T, s) = n_{tot} \mu_{DG} + n_{H_2O} \mu_W + \tau_{LS} A_S. \quad (32)$$

In Eq. (32) the total gas mole number of the system is given by  $n_{tot}$  and  $n_{H_2O}$  that of water and its vapor,  $\mu_{DG}$  and  $\mu_W$  are the chemical potentials of the dissolved gas and water respectively. Note that in order to obtain an equilibrated state, an energy minimum of the system, the first-order variation of the total free energy should be set to zero i.e.  $\delta G_{tot} = 0$ , where classical geometry formulas (Frankel, 2011; Giacomello et al., 2012) are used to obtain:

$$\delta G_{tot} = (p_L - p_G - p_V) \delta V_G + \tau_{LG}(\delta A_{LG} + \delta A_{SG} \cos \theta_Y) + RT \ln \frac{p_G}{s(p_L - p_V^*)} \delta n_G + RT \ln \frac{p_V}{p_V^*} \delta n_V. \quad (33)$$

The variation with respect to the first and second term determines the shape and location of the interface since it results in the Young-Laplace equation:

$$p_L - p_G - p_V = -\tau_{LG} \kappa. \quad (34)$$

The third term gives the variation with respect to  $\delta n_G$ , which is the chemical equilibrium condition between the free and dissolved gas in water:

$$p_G = s(p_L - p_V^*). \quad (35)$$

The fourth term gives the variation with respect to  $\delta n_V$ , which is the equilibrium equation between vapor and water:

$$p_V = p_V^*. \quad (36)$$

### 3.1. Overview of Gibbs free energy in a Variation Level Set Formulation

Define an energy functional  $\mathcal{E}(\phi)$  where  $\phi(\mathbf{x}, t) > 0$  represents the liquid phase,  $\phi(\mathbf{x}, t) < 0$  represents the gas phase and  $\phi(\mathbf{x}, t) = 0$  represents the liquid-gas interface. Define another level set  $\psi(\mathbf{x})$  that represents the solid roughness,

$\psi(\mathbf{x}) \geq 0$  for the region inside the solid substrate and  $\psi(\mathbf{x}) < 0$  outside the solid. Then,  $\mathcal{E}(\phi)$  based on the bulk and interfacial energies can be written as:

$$\mathcal{E}(\phi) = \mathcal{E}_{\mathcal{B}}(\phi) + \mathcal{E}_{\mathcal{I}}(\phi), \quad (37)$$

where  $\mathcal{E}_{\mathcal{B}}(\phi)$  and  $\mathcal{E}_{\mathcal{I}}(\phi)$  are the bulk and interfacial surface energy respectively. Using Eq. (31), the bulk energy due to the pressure difference is given by  $\mathcal{E}_{\mathcal{B}} = (p_L - p_G - p_V)V_G$ . Denote  $\Delta p = p_G + p_V - p_L$  then substitute Eq. (35) and Eq. (36) to get  $\Delta p = (1 - s)(p_V - p_L)$ . Using Eq. (6), the following is obtained:

$$\mathcal{E}_{\mathcal{B}}(\phi) = - \int_{\Omega} \Delta p H(-\psi(\mathbf{x})) H(\phi(\mathbf{x}, t)) \, d\mathbf{x}, \quad (38)$$

where  $H(-\psi(\mathbf{x}))$  ensures that the pressure difference is only applied outside the solid region. The energy functional due to the interfacial surface energies from Eq. (31) is given by  $\mathcal{E}_{\mathcal{I}} = \tau_{LG}(A_{LG} + A_{SG} \cos \theta_Y)$ . Note that the contact angle satisfies  $\tau_{LS} - \tau_{SG} = \tau_{LG} \cos \theta_Y$ . If  $0 \leq \theta_Y \leq \pi/2$ , then the liquid is said to be wetted, else if  $\pi/2 < \theta_Y \leq \pi$ , then the liquid is said to be non-wetted. The surface tension is represented as a function of  $\psi(\mathbf{x})$  such that,

$$\tau(\psi) = \begin{cases} \tau^+ & \text{for } \psi(\mathbf{x}) \geq 0, \\ \tau^- & \text{for } \psi(\mathbf{x}) < 0, \end{cases} \quad (39)$$

where  $\tau^+ = |\tau_{LS} - \tau_{SG}|$  and  $\tau^- = \tau_{LG}$ . Using Eq. (10), the interfacial surface energy is written as

$$\mathcal{E}_{\mathcal{I}}(\phi) = \int_{\Omega} \tau(\psi(\mathbf{x})) \delta(\phi(\mathbf{x}, t)) |\nabla \phi(\mathbf{x}, t)| \, d\mathbf{x}. \quad (40)$$

Since the solid does not vary temporally, substitute  $\tau(\psi(\mathbf{x}))$  for  $\tau(\mathbf{x})$ :

$$\mathcal{E}_{\mathcal{I}}(\phi) = \int_{\Omega} \tau(\mathbf{x}) \delta(\phi(\mathbf{x}, t)) |\nabla \phi(\mathbf{x}, t)| \, d\mathbf{x}. \quad (41)$$

The interface is not allowed to penetrate into the solid, therefore a no penetration constraint is enforced:

$$\mathcal{G}_1(\phi) = \int_{\Omega} H(-\phi(\mathbf{x}, t)) H(\psi(\mathbf{x})) \, d\mathbf{x} = 0; \quad (42)$$

this prevents any overlap or penetration between the two regions described by  $\phi(\mathbf{x}, t) \geq 0$  and  $\psi(\mathbf{x}) \geq 0$ . The volume of the liquid phase is required to remain conserved, therefore the second constraint imposed is volume conservation given by:

$$\mathcal{G}_2(\phi) = \int_{\Omega} H(\phi(\mathbf{x}, t)) H(-\psi(\mathbf{x})) \, d\mathbf{x} = V_o, \quad (43)$$

where  $V_o$  is the initial volume of the liquid. This is necessary for problems which require the conservation of the volume of the bubble. For problems where we assume an infinite supply of liquid (i.e. a system where the liquid reservoir is much larger than the air cavities), this constraint is not used. In order to minimize  $\mathcal{E}(\phi)$ , we define the auxiliary energy function  $\mathcal{J}(\phi)$  that contains the Gibbs energy, penalty function and the two constraints, given by:

$$\mathcal{J}(\phi) = \alpha \mathcal{R}_p(\phi) + \mathcal{E}(\phi) + \mu \mathcal{G}_1(\phi) + \lambda \mathcal{G}_2(\phi), \quad (44)$$

where  $\mathcal{R}_p(\phi)$  is the penalty term that enforces  $\phi$  to be a SDF in the vicinity of the interface,  $\alpha$  is the weighting and  $\mu$  and  $\lambda$  are the Lagrange multipliers that satisfy the two constraints mentioned above. Then the Fréchet derivative in

the  $L^2$  norm of  $\mathcal{J}(\phi)$  is given by:

$$\lim_{\epsilon \rightarrow 0} \frac{1}{\epsilon} \left[ \mathcal{J}(\phi + \epsilon\chi) - \mathcal{J}(\phi) \right] = \left\langle \frac{\partial \mathcal{J}}{\partial \phi}, \chi \right\rangle = \left\langle \frac{\partial \mathcal{R}_p}{\partial \phi}, \chi \right\rangle + \left\langle \frac{\partial \mathcal{E}_I}{\partial \phi}, \chi \right\rangle + \left\langle \frac{\partial \mathcal{E}_B}{\partial \phi}, \chi \right\rangle + \left\langle \frac{\partial \mathcal{G}_1}{\partial \phi}, \chi \right\rangle + \left\langle \frac{\partial \mathcal{G}_2}{\partial \phi}, \chi \right\rangle. \quad (45)$$

The first term in the right-hand side  $\left\langle \frac{\partial \mathcal{J}}{\partial \phi}, \chi \right\rangle$  is given in Eq. (24). The second term can be shown to be:

$$\left\langle \frac{\partial \mathcal{E}_I}{\partial \phi}, \chi \right\rangle = \int_{\partial\Omega} \delta(\phi(\mathbf{x}, t)) \frac{\partial \phi(\mathbf{x}, t)}{\partial n} \frac{\tau(\mathbf{x})}{|\nabla \phi(\mathbf{x}, t)|} \chi \, ds - \int_{\Omega} \delta(\phi(\mathbf{x}, t)) \nabla \cdot \left( \tau(\mathbf{x}) \frac{\nabla \phi(\mathbf{x}, t)}{|\nabla \phi(\mathbf{x}, t)|} \right) \chi \, d\mathbf{x}, \quad (46)$$

where the first term is eliminated by taking  $\frac{\partial \phi}{\partial n} = 0$  at the boundaries  $\partial\Omega$ . The rest of the terms follow as:

$$\left\langle \frac{\partial \mathcal{E}_B}{\partial \phi}, \chi \right\rangle = - \int_{\Omega} \Delta p \delta(\phi(\mathbf{x}, t)) H(-\psi(\mathbf{x})) \chi \, d\mathbf{x}, \quad (47)$$

$$\left\langle \frac{\partial \mathcal{G}_1}{\partial \phi}, \chi \right\rangle = - \int_{\Omega} \delta(\phi(\mathbf{x}, t)) H(\psi(\mathbf{x})) \chi \, d\mathbf{x}, \quad (48)$$

and

$$\left\langle \frac{\partial \mathcal{G}_2}{\partial \phi}, \chi \right\rangle = \int_{\Omega} \delta(\phi(\mathbf{x}, t)) H(-\psi(\mathbf{x})) \chi \, d\mathbf{x}. \quad (49)$$

The evolution equation given by Eq. (18) can now be defined for an infinitesimal step-size as:

$$\frac{\partial \phi(\mathbf{x}, t)}{\partial t} = \alpha \nabla \cdot \left( d_p(|\nabla \phi(\mathbf{x}, t)|) \nabla \phi(\mathbf{x}, t) \right) + \delta(\phi(\mathbf{x}, t)) \left[ \nabla \cdot \left( \tau(\mathbf{x}) \frac{\nabla \phi(\mathbf{x}, t)}{|\nabla \phi(\mathbf{x}, t)|} \right) + \Delta p H(-\psi(\mathbf{x})) + \mu H(\psi(\mathbf{x})) - \lambda H(-\psi(\mathbf{x})) \right]. \quad (50)$$

To determine the value of the Lagrange multipliers, we enforce the fact that the constraints do not vary in time, i.e.

$$\frac{d}{dt} \mathcal{G}_1(\phi) = 0 \quad (51)$$

$$\frac{d}{dt} \mathcal{G}_2(\phi) = 0. \quad (52)$$

Therefore, the Lagrange multipliers can be obtained as:

$$\mu = - \frac{\int_{\Omega} \delta(\phi(\mathbf{x}, t)) \left[ \alpha \nabla \cdot \left( d_p(|\nabla \phi(\mathbf{x}, t)|) \nabla \phi(\mathbf{x}, t) \right) + \delta(\phi(\mathbf{x}, t)) \nabla \cdot \left( \tau(\mathbf{x}) \frac{\nabla \phi(\mathbf{x}, t)}{|\nabla \phi(\mathbf{x}, t)|} \right) \right] H(\psi(\mathbf{x})) \, d\mathbf{x}}{\int_{\Omega} \delta^2(\phi(\mathbf{x}, t)) H(\psi(\mathbf{x})) \, d\mathbf{x}}, \quad (53)$$

and

$$\lambda = \frac{\int_{\Omega} \delta(\phi(\mathbf{x}, t)) \left\{ \alpha \nabla \cdot \left( d_p(|\nabla \phi(\mathbf{x}, t)|) \nabla \phi(\mathbf{x}, t) \right) + \delta(\phi(\mathbf{x}, t)) \left[ \nabla \cdot \left( \tau(\mathbf{x}) \frac{\nabla \phi(\mathbf{x}, t)}{|\nabla \phi(\mathbf{x}, t)|} \right) + \Delta p \right] \right\} H(-\psi(\mathbf{x})) \, d\mathbf{x}}{\int_{\Omega} \delta^2(\phi(\mathbf{x}, t)) H(-\psi(\mathbf{x})) \, d\mathbf{x}}. \quad (54)$$

The above equations use the fact that

$$H(\psi(\mathbf{x})) H(-\psi(\mathbf{x})) = 0, \quad (55)$$

$$H^2(\psi(\mathbf{x})) = H(\psi(\mathbf{x})). \quad (56)$$

Note that at steady state, equilibrium is reached (i.e.  $\partial \phi / \partial t = 0$  and  $\lambda = 0$ ). Assuming no solid is present (i.e.  $\mu = 0$ ) and  $\tau(\mathbf{x}) = \tau_{LG}$ , we get the following:

$$\Delta p = \tau_{LG} \nabla \cdot \left( \frac{\nabla \phi(\mathbf{x}, t)}{|\nabla \phi(\mathbf{x}, t)|} \right). \quad (57)$$

The Young-Laplace equation in Eq. (34) is recovered.

#### 4. Numerical Implementation

In practice, the Heaviside function  $H(\phi)$  and the delta function  $\delta(\phi)$  are slightly smoothed out such that:

$$H_\epsilon(\phi) = \begin{cases} 1 & \text{if } \phi > \epsilon, \\ \frac{1}{2} \left[ 1 + \frac{\phi}{\epsilon} + \frac{1}{\pi} \sin\left(\frac{\pi\phi}{\epsilon}\right) \right] & \text{if } |\phi| \leq \epsilon, \\ 0 & \text{if } \phi < -\epsilon \end{cases} \quad (58)$$

and

$$\delta_\epsilon(\phi) = \begin{cases} 0 & \text{if } |\phi| > \epsilon, \\ \frac{1}{2\epsilon} \left[ 1 + \cos\left(\frac{\pi\phi}{\epsilon}\right) \right] & \text{if } |\phi| \leq \epsilon; \end{cases} \quad (59)$$

where  $\epsilon$  is the numerical width of  $\delta(\phi)$  and  $H(\phi)$  taken to be slightly larger than the width of a grid cell ( $\epsilon = 1.5\Delta x$ ). The DRLSE can be implemented with a simple finite difference scheme. The spatial gradients  $\partial\phi/\partial x_i$  are obtained by using a central difference scheme and the temporal partial derivative  $\partial\phi/\partial t$  is approximated using forward difference. Heun's method is also implemented so that we obtain a second-order approximation with a slightly less Courant-Friedrichs-Lewy (CFL) restriction. The evolution equation is discretized for the forward Euler as,

$$\phi_{i,j,k}^{n+1} = \phi_{i,j,k}^n + \delta t L(\phi_{i,j,k}^n), \quad (60)$$

and for Heun's method as

$$\bar{\phi}_{i,j,k}^{n+1} = \phi_{i,j,k}^n + \delta t L(\phi_{i,j,k}^n) \quad (61)$$

$$\phi_{i,j,k}^{n+1} = \frac{1}{2} \phi_{i,j,k}^n + \frac{1}{2} \bar{\phi}_{i,j,k}^{n+1} + \delta t L(\bar{\phi}_{i,j,k}^n). \quad (62)$$

The key difference here is the fact that the operator  $L[\phi]$  in the variational formulation here does not describe a Hamilton-Jacobi equation with a curvature regularization of the traditional formulation but a reaction-diffusion type problem. Here the LSE equation is written out explicitly as:

$$\frac{\partial\phi}{\partial t} = \alpha \nabla \cdot (d_p(|\nabla\phi|)\nabla\phi) + \delta(\phi) \left[ \tau \nabla \cdot \left( \frac{\nabla\phi}{|\nabla\phi|} \right) + \nabla\tau \cdot \frac{\nabla\phi}{|\nabla\phi|} + H(-\psi)\Delta p + \mu H(\psi) + \lambda H(-\psi) \right], \quad (63)$$

where there is no need for reinitialization or replacing  $\delta(\phi)$  with  $|\nabla\phi|$ . This allows for the flexibility of initializing  $\phi$  as a binary function. The initial condition LS does not necessarily have to be a signed distance function,  $|\nabla\phi| = 1$  is only enforced in the vicinity of  $\phi = 0$  where  $\delta(\phi)$  is active. It suffices to define a divergence function  $div(\cdot)$  that can be used for both the regularization term and the normals to obtain curvature which is simply given by  $\kappa = \nabla \cdot \mathbf{N}$ . Some attention to detail of implementation was required for the Lagrange multipliers. The term in the denominator of the Lagrange multipliers  $\mu$  given in Eq. (64) causes leakage since the width of  $\delta(\phi)$  becomes too narrow; the term  $\delta^2(\phi)$  is replaced with  $\delta(\phi)|\nabla\phi|$ . Numerically, the assumptions in Eq. (55) and Eq. (56) do not hold. This is inconsequential when there is no requirement for volume conservation since  $\lambda = 0$ . However for cases where volume conservation is required, it is important to keep their product explicitly in the discretized equations so that the equations balance out. Otherwise, the diffusion term causes the interface to eventually disappear. Therefore, the discrete Lagrange

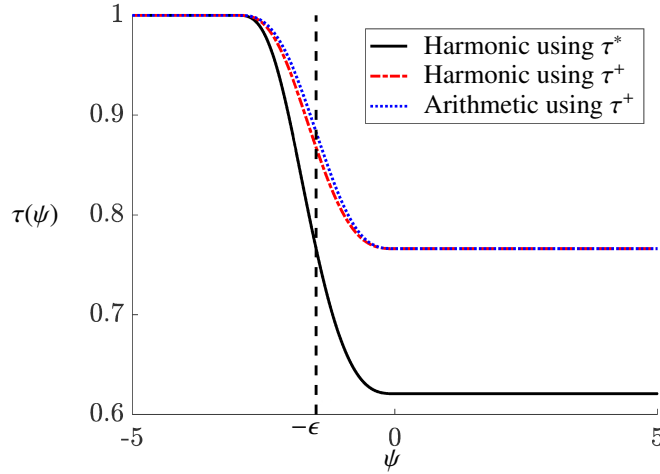


Fig. 2: Surface tension distribution using the traditional arithmetic mean with  $\tau^+$  (dashed blue line), harmonic mean with  $\tau^+$  (dash-dot red line) and harmonic mean with  $\tau^*$  (solid black line). The solid interface location is denoted by the vertical dashed line at  $\psi = -\epsilon$ . The illustrated example uses  $\tau^- = 1$  and  $\tau^+ = -\cos \theta_Y$  where  $\theta_Y = 140^\circ$ .

multipliers are written as:

$$\mu = - \frac{\int_{\Omega} \delta(\phi) \left\{ \alpha \nabla \cdot (d_p(|\nabla \phi|) \nabla \phi) + \delta(\phi) \left[ \tau \nabla \cdot \left( \frac{\nabla \phi}{|\nabla \phi|} \right) + \nabla \tau \cdot \frac{\nabla \phi}{|\nabla \phi|} + \Delta p H(-\psi) + \lambda H(-\psi) \right] \right\} H(\psi) \, dx}{\int_{\Omega} \delta(\phi) |\nabla \phi| H(\psi) \, dx}, \quad (64)$$

and

$$\lambda = \frac{\int_{\Omega} \delta(\phi) \left\{ \alpha \nabla \cdot (d_p(|\nabla \phi|) \nabla \phi) + \delta(\phi) \left[ \tau \nabla \cdot \left( \frac{\nabla \phi}{|\nabla \phi|} \right) + \nabla \tau \cdot \frac{\nabla \phi}{|\nabla \phi|} + \Delta p H(-\psi) + \mu H(\psi) \right] \right\} H(-\psi) \, dx}{\int_{\Omega} \delta^2(\phi) H^2(-\psi) \, dx}. \quad (65)$$

The surface tension values are different for the interface between the liquid and gas, and the liquid and solid. Prescribing a binary distribution for  $\tau(\mathbf{x})$  given by Eq. (39) leads to a stair-casing effect. Similar to Zhao et al. (1998), surface tension is given as a distribution with a slight shift in the argument of the Heaviside function to move the stiffest change away from the solid boundary,

$$\tau(\mathbf{x}) = \tau^+ + (\tau^- - \tau^+) H(-\psi - \epsilon). \quad (66)$$

In the paper by Zhao et al. (1998), the bubble shape at equilibrium was not compared to a analytic solution and the contact angle at the triple-line junction was not reported. Qualitatively, the results were promising and demonstrated the effectiveness of the method. However, in our experience, the surface tension distribution caused the interface location to have a mismatch when compared to analytic solution, with errors ranging between 2% to 8%. The reason for this error is due to the smoothing of the Heaviside function. At equilibrium, the Heaviside function at the interface location has a value of  $H(\phi) = 0.5$ , this leads to an under predicted value of  $\tau^+$  at the solid interface causing a mismatch in the contact angle and in turn the equilibrium position. To remedy this effect, we found that a temporary surface tension value  $\tau^*$  can be defined such that the correct value of surface tension with the solid is obtained at the

interface location. A harmonic mean is used in Eq. (66) to further reduce any errors that stem from the lower value of the dummy variable. The surface tension distribution becomes as follows

$$\tau(\mathbf{x}) = \left[ \frac{H(-\psi - \epsilon)}{\tau^-} + \frac{1 - H(-\psi - \epsilon)}{\tau^*} \right]^{-1}, \quad (67)$$

where

$$\tau^* = \frac{\tau^+ \tau^-}{2\tau^- - \tau^+}. \quad (68)$$

Note that substituting Eq. (68) in Eq. (67) gives the desired value of  $\tau(\mathbf{x}) = \tau^-$  at the interface where  $H(\phi) = 0.5$ . Although the value inside the solid is incorrect, the value remains inconsequential since the no penetration constraint and the formulation are only relevant outside the solid. Figure 2 presents a comparison between the different methods. The harmonic mean using  $\tau^*$  achieves the desired value of  $\tau^+$  at a faster rate for a given interface location. The pseudo-code is summarized in Algorithm 1:

---

**Algorithm 1** Pseudo-code using Heun's method

---

- 1: Initialize  $\Phi^0 := \{\phi_{i,j,k}^0\}_{i,j,k=1}^{n_x, n_y, n_z}$ . Choose  $\tau^+$ ,  $\tau^-$ ,  $\alpha$ ,  $\delta t$  and  $T$ .
  - 2: Set the solid boundary  $\psi$ .
  - 3: Calculate surface tension distribution using Harmonic mean with  $\tau^*$
  - 4: Compute  $H_\psi := H_\epsilon(\psi)$ ,  $\tau_\psi := \tau(\psi)$  and  $H_{-\psi} := H_\epsilon(-\psi)$ .
  - 5: **for**  $n = 1$  to  $T$  **do**
  - 6:   **for**  $k = 1$  to  $n_z$  **do**
  - 7:     **for**  $j = 1$  to  $n_y$  **do**
  - 8:      **for**  $i = 1$  to  $n_x$  **do**
  - 9:        $\bar{\phi}_{ijk}^{n+1} = \phi_{ijk}^n + \delta t \mathbf{L}[\phi_{ijk}^n]$
  - 10:        $\phi_{ijk}^{n+1} = \frac{1}{2}\phi_{ijk}^n + \frac{1}{2}\bar{\phi}_{ijk}^{n+1} + \frac{1}{2}\delta t \mathbf{L}[\bar{\phi}_{ijk}^{n+1}]$
  - 11:      **end for**
  - 12:     **end for**
  - 13:   **end for**
  - 14: **return**
  - 15: Define  $f = \mathbf{L}(\phi)$
  - 16: Define  $\text{div}(\cdot) = \nabla \cdot (\cdot)$
  - 17: Compute the discrete  $\delta_\phi := \delta_\epsilon(\phi)$  and  $H_\phi := H_\epsilon(\phi)$ .
  - 18: Compute gradients  $\nabla\phi = \partial\phi/\partial x_i$  using central difference.
  - 19: Compute magnitude of the gradient  $|\nabla\phi| = \sqrt{(\partial\phi/\partial x)^2 + (\partial\phi/\partial y)^2 + (\partial\phi/\partial z)^2}$ .
  - 20: Compute normals  $\mathbf{N} = \nabla\phi/|\nabla\phi|$ .
  - 21: Compute the penalty term  $\mathcal{R}_p(\phi) := \alpha \text{div}(d_p(|\nabla\phi|)\nabla\phi)$ .
  - 22: Compute curvature term  $\kappa(\phi) := \text{div}(\mathbf{N})$  using central difference.
  - 23: Compute gradient of surface tension distribution  $\nabla\tau$  using central difference.
  - 24: Compute Lagrange multipliers  $\lambda(\phi)$ ,  $\mu(\phi)$  using trapezoidal rule.
  - 25: Set  $f = R_p(\phi) + \delta_\phi[\tau\kappa(\phi) + \nabla\tau \cdot \mathbf{N} + H_{-\psi}\Delta p + \mu(\phi)H_\psi + \lambda(\phi)H_{-\psi}]$
  - 26: **end for**
  - 27: **return**
- 

*Remark.* In the formulation by Zhao et al. (1998), the traditional level set is employed; the evolution of  $\phi$  given by Eq. (57) and  $\delta(\phi)$  is replaced by  $|\nabla\phi|$ . Note that the operator  $\mathbf{L}[\phi]$  in section §2.1 describes a convection-diffusion equation given in Eq. (11). The system of LSE contains Hamilton-Jacobi equations coupled to curvature and stiff source terms. Singularities may develop in the solution and the numerical implementation requires much of the modern level set

technology to obtain a stable solution (Zhao et al., 1996). The crucial ingredients are:

- (i) Break up the parabolic and hyperbolic terms and address each one with the appropriate numerical discretization.
- (ii) High order accurate essentially non-oscillatory schemes (originating in the study of hyperbolic conservation laws) developed for Hamilton-Jacobi equations.
- (iii) Re-initialization of each LSF to be a SDF using Eq. (13).
- (iv) The curvature definition uses the explicit term involving the gradients of  $\phi$  given by:

$$\kappa = (\phi_x^2 \phi_{yy} - 2\phi_x \phi_y \phi_{xy} + \phi_y^2 \phi_{xx} + \phi_x^2 \phi_{zz} - 2\phi_x \phi_z \phi_{xz} + \phi_z^2 \phi_{xx} + \phi_y^2 - 2\phi_y \phi_z \phi_{yz} + \phi_z^2 \phi_{yy}) / |\nabla \phi|^3. \quad (69)$$

However, the Lagrange multiplier requires the use of a distance function to define curvature on or near the front using a separate definition given by:

$$\kappa = \text{trace}[[I - \phi D^2 \phi]^{-1} D^2 \phi], \quad (70)$$

where  $D^2 \phi$  is the Hessian of  $\phi$ . This formulae yields a constant value of  $\kappa$  normal to the front and gives the correct value on the front.

## 5. Validation

We begin with the effect of distance regularization as a method to satisfy  $|\nabla \phi| = 1$ , next we build up in complexity of the evolution equation where we make sure that this method can solve the traditional level set problems such motion in the normal direction and curvature driven flows. We validate our energy minimization model of the Gibbs free energy with the analytic solution of Carbone and Mangialardi (2005). Then we finally present some results over general geometries to demonstrate the effectiveness and flexibility of the proposed solver.

### 5.1. Distance Regularization as reinitialization

The effect of distance regularization as a method of reinitialization is demonstrated by simulating the forward and backward (FAB) diffusion problem with a binary level set function. Define the initial binary level set function  $\phi_o$  by

$$\phi_o(\mathbf{x}) = \begin{cases} -c_o, & \text{for } \mathbf{x} \in \Omega_o \\ 0, & \text{for } \mathbf{x} \in \partial\Omega_o \\ c_o, & \text{for } \mathbf{x} \in \Omega - \Omega_o \end{cases} \quad (71)$$

where  $c_o$  is a positive constant. Note that  $\phi_o$  does not need not be initialized as a signed distance function like traditional level set methods; this allows for flexibility in initialization due to its simplicity and practicality. The region  $\Omega_o$  is taken to be a square of side length 60 embedded in a square domain on a  $100 \times 100$  grid. Define  $\phi_o$  with a constant of  $c_o = 10$  which creates a steep jump of  $2c_o$  as shown in figure 3(a), the solid red line highlights the zero crossing of  $\phi_o$ . The evolution of  $\phi$  follows from the description of the properties of double-well potential given in section 2.2.1. We solve a simple FAB diffusion evolution equation given by

$$\frac{\partial \phi}{\partial t} = -\frac{\partial \mathcal{J}}{\partial \phi} = -\alpha \frac{\partial \mathcal{R}_p}{\partial \phi} = \alpha \nabla \cdot (d_p(|\nabla \phi|) \nabla \phi) \quad (72)$$

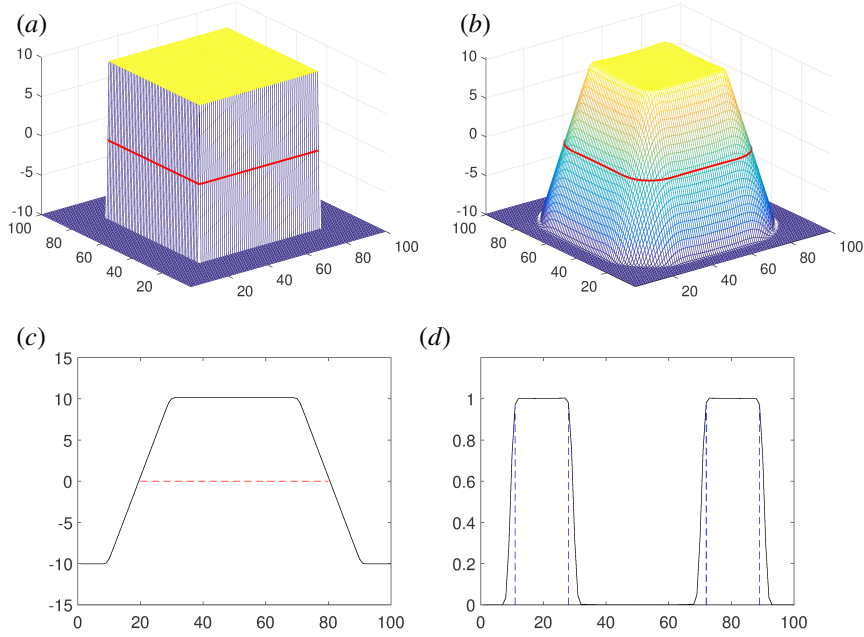


Fig. 3: The evolution of a level set function under the effect of distance regularization. (a) The initial level set  $\phi_o$  where the red solid line indicates  $\phi_o = 0$ . (b) The final level set after diffusion where the solid red line indicates  $\phi = 0$ . (c) A cross-section of the final level set function where the red dashed line indicates  $\phi = 0$ . (d) A cross-section of  $|\nabla\phi|$  where the blue dashed lines indicate the width of the signed distance band.

At  $t = 0$  the zero crossing of  $\phi_o$  has a  $|\nabla\phi_o| \gg 1$  due to the steep jump in the binary initialization. As a result, the diffusion rate  $\alpha d_p(|\nabla\phi|)$  is positive and drives a forward diffusion which reduces  $|\nabla\phi|$  until it reaches unity; the forward diffusion stops once  $|\nabla\phi| = 1$ . For the case where  $|\nabla\phi|$  becomes less than unity, then  $\alpha d_p(|\nabla\phi|)$  becomes negative for  $(1/2) < |\nabla\phi| < 1$ , therefore the backward diffusion increases the value of  $|\nabla\phi|$  to unity. Figure 3(b) shows the final result of  $\phi$  where the level set is a signed distance function in the vicinity of the zero level set crossing. Figure 3(c) shows a cross section of  $\phi$  for  $y = 50$  where the dashed red line indicates the zero crossing. Note that  $|\nabla\phi| = 1$  is satisfied within  $c_o$  and  $-c_o$  about the zero crossing, which will be defined as the signed distance band (SDB). Figure 3(d) shows a cross section of  $|\nabla\phi|$  where the SDB, of width approximately  $2c_o$ , is highlighted with the dashed blue lines. On either sides of the SDB the binary function is constant, therefore  $|\nabla\phi| = 0$  and  $\alpha d_p(|\nabla\phi|) > 0$  indicating a forward diffusion that keeps  $\phi$  flat at its constant value since the double-well potential is at a minimum.

## 5.2. Curvature driven flow

Traditional level set method has been used extensively in the context of an externally driven flow. This involves both an externally generated velocity field, or a self-generated field  $\mathbf{u}$  that depends directly on  $\phi$ . Consider the motion by mean curvature where the interface moves in the normal direction to the interface with a velocity proportional to its curvature. The velocity field is defined by  $\mathbf{u} = -\kappa \mathbf{N}$  where  $\kappa = \nabla \cdot (\nabla\phi/|\nabla\phi|)$  such that the evolution equation becomes

$$\frac{\partial\phi}{\partial t} - \kappa \mathbf{N} \cdot \nabla\phi = 0, \quad (73)$$

which is equivalent to

$$\frac{\partial \phi}{\partial t} - \kappa |\nabla \phi| = 0. \quad (74)$$

since the normal  $\mathbf{N}$  is along the gradient direction  $\nabla \phi$ . The above results in a parabolic equation  $\phi_t = \kappa |\nabla \phi|$  that can be solved using central differencing with a stringent time-step restriction for stability. In the context of variational level set methodology, we can show that a mean curvature flow can be obtained from minimizing an external energy defined by the surface area of the level set given by

$$\mathcal{E}_{ext}(\phi) = L_0(\phi) = \int_{\Omega} \delta(\phi) |\nabla \phi| \, d\mathbf{x}. \quad (75)$$

Taking the Fréchet derivative of  $\mathcal{E}_{ext}$  with respect to the  $L^2$  inner product gives

$$\frac{\partial \mathcal{E}_{ext}}{\partial \phi} = -\delta(\phi) \nabla \cdot \left( \frac{\nabla \phi}{|\nabla \phi|} \right). \quad (76)$$

This is similar to the curvature driven evolution equation with the exception of  $\delta(\phi)$  is  $|\nabla \phi|$  instead. Zhao et al. (1998) simply replaced the terms in his formulation and reasoned that using  $|\nabla \phi|$  is less stiff. Although the both evolution equations are curvature driven, it is worth pointing out that they are inherently different. The equation given by  $\phi_t = \delta(\phi) \nabla \cdot (\nabla \phi / |\nabla \phi|)$  moves the zero level set only which is only active due to  $\delta(\phi)$ . However, the equation given by  $\phi_t = |\nabla \phi| \nabla \cdot (\nabla \phi / |\nabla \phi|)$  moves all the level sets by their respective curvatures i.e. all the neighboring values of the level set evolve with the same law. Esodoglu et al. (2008) argues that by definition, we can allow all the level sets to move by a perturbation for an energy functional that measures the total length of all level curves

$$\mathcal{E}_{ext}(\phi) = \int_{\beta} L_{\beta}(\phi) \, d\beta = \int_{\Omega} |\nabla \phi| \, d\mathbf{x}, \quad (77)$$

where  $\int_{\beta} L_{\beta}(\phi) \, d\beta = \int_{\beta} \int_{\Omega} L(\phi - \beta) \, d\beta \, d\mathbf{x}$ . Note that the variation of  $\phi$  only affects  $\nabla \phi$  but does not move the level sets. Since the level set is a signed distance function, we can define a new level set norm (Esodoglu et al., 2008) instead of the usual  $L^2$  norm as

$$\langle f, g \rangle_{\phi} = \int_{\Omega} f \frac{g}{|\nabla \phi|} \, d\mathbf{x}. \quad (78)$$

The Fréchet derivative obtained from this new norm is

$$\lim_{\epsilon \rightarrow 0} \frac{1}{\epsilon} \left[ \mathcal{E}_{ext}(\phi + \epsilon \chi) - \mathcal{E}_{ext}(\phi) \right] = \left\langle \frac{\partial \mathcal{E}_{ext}}{\partial \phi}, \chi \right\rangle_{\phi} = - \int_{\Omega} \nabla \cdot \left( \frac{\nabla \phi}{|\nabla \phi|} \right) |\nabla \phi| \frac{\chi}{|\nabla \phi|} \, d\mathbf{x}, \quad (79)$$

This results in

$$\frac{\partial \mathcal{E}_{ext}}{\partial \phi} = -\nabla \cdot \left( \frac{\nabla \phi}{|\nabla \phi|} \right) |\nabla \phi|, \quad (80)$$

which lends itself to the traditional curvature driven flow discussed earlier in this section. The evolution equation solved is given by

$$\frac{\partial \phi}{\partial t} = \alpha \nabla \cdot (d_p(|\nabla \phi|) \nabla \phi) + \nabla \cdot \left( \frac{\nabla \phi}{|\nabla \phi|} \right) |\nabla \phi|. \quad (81)$$

Here we like to note the following, as mentioned earlier we can advect all the level curves in the context of energy minimization such that we can replicate the motion of a curvature driven flow. Isolating the zero level set curve gives

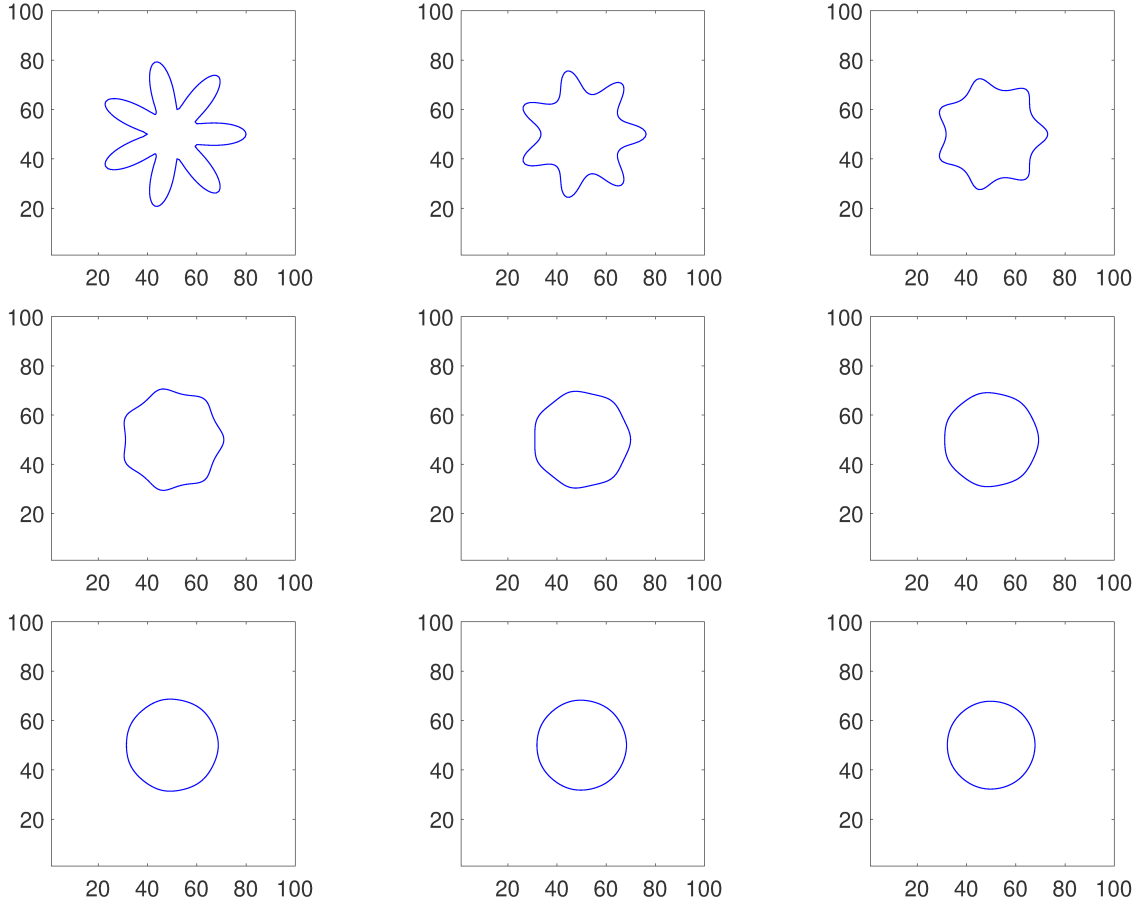


Fig. 4: Evolution of the star-shape under a curvature-driven flow. The images are snapshots in time from left to right, top to bottom where the star collapses unto a circle for  $t = 0.0, 7.5, 15.0, 22.5, 30.0, 37.5, 45.0, 52.5, 60.0$ .

an evolution equation that does not look like the typical curvature driven flow, but since the current method is only concerned with the region around the interface only, it is able to handle both equations without running into stability issues. This was tested for both formulations but we will only present the traditional cases for brevity. The only difference observed between the two formulations is the rate at which the curves reach the desired final solution.

### 5.2.1. Seven-pointed Star

Consider a seven pointed star given by the following parametrized curve

$$\gamma(s) = [20 + 10 \cos(7 \cdot 2\pi s)][\cos(2\pi s), \sin(2\pi s)] \quad \text{for } s \in [0, 1], \tag{82}$$

such that the zero level set is defined from polar coordinates is given by

$$\phi(\mathbf{x}, 0) = \|\mathbf{x} - \mathbf{x}_c\| - \left\{ 20 + 10 \cos \left[ 7 \cdot \arctan \left( (y - y_c) / (x - x_c) \right) \right] \right\}, \tag{83}$$

where  $\mathbf{x}_c$  is the offset parameter. We shift the petal shapes of the star from its center by 20 units of length which effectively increases the relative size of the points compared to the main body, a scaling factor of 10 for the star size

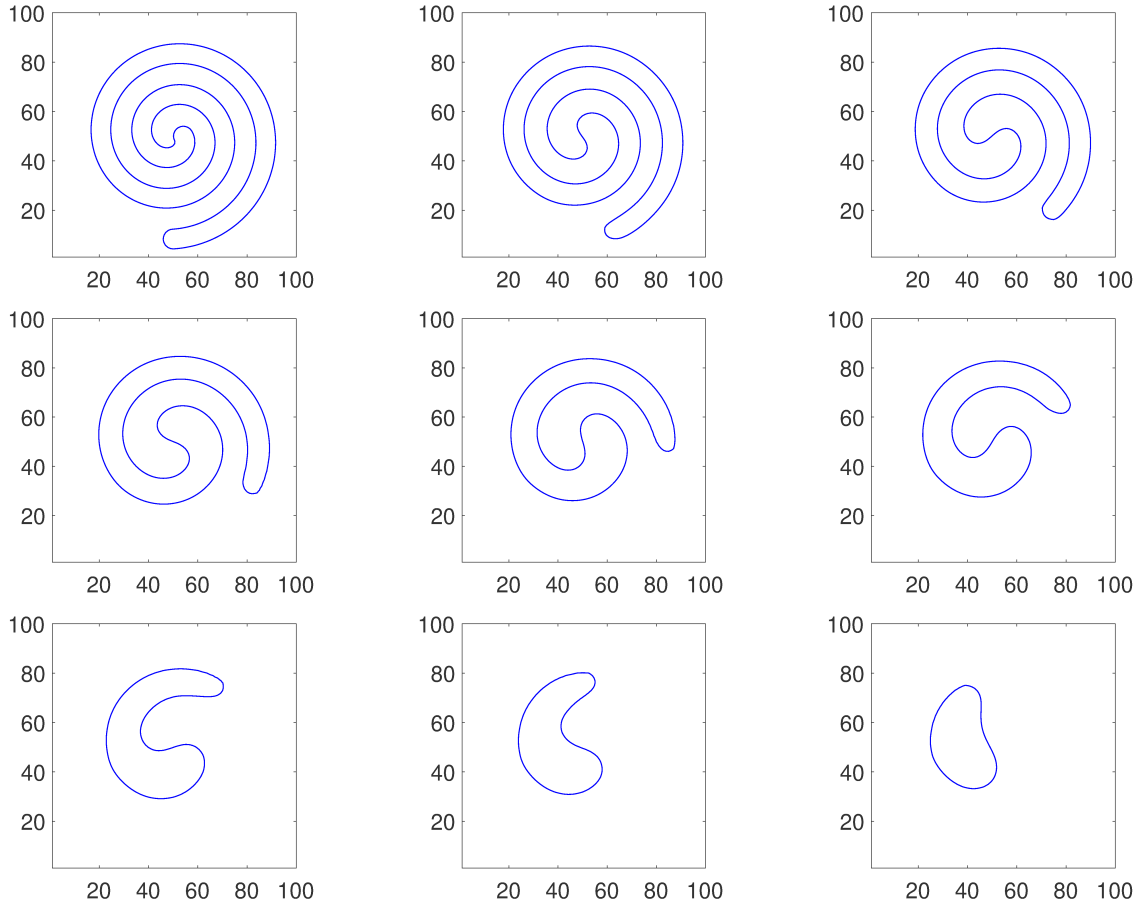


Fig. 5: Evolution of the spiral under a curvature-driven flow. The images are snapshots in time from left to right, top to bottom where the ends of the spiral unwind faster than the interior region for  $t = 0.0, 37.5, 75.0, 112.5, 150.0, 187.5, 225.0, 262.5, 300.0$ .

and 7 points for the star. The computational domain is a square with side length of a 100 units and a grid size of  $100 \times 100$ . The time step is  $dt = 0.1$  and  $\alpha = 0.4$ . The star-shaped level curve is centered at  $(50, 50)$ . The code is run for 600 iterations. Figure 4 shows the progression of the front evolving under the curvature-driven flow for  $t = 0.0, 7.5, 15, 22.5, 30.0, 37.5, 45.0, 52.5, 60.0$ . The star-shaped curve collapses to circle under this motion where the region of positive curvature (peaks) collapses inwards and the regions of negative curvature (troughs) propagate outward.

### 5.2.2. Wound Spiral

Figure 5 shows the results of the same curvature-driven motion for a wound spiral given by the following parametrization

$$\theta = 2\pi D \sqrt{s} \quad \text{for } s \in [0, 1], \quad (84)$$

such that  $s = (k + a)/(np + a)$  where  $k$  is an integer that loops over from the first point to the total number of points  $np$ , and the value of  $a$  determines the shape of the spiral head in the center. The location of the points are defined by

$$x_p = x_c + sf [D/(1 + D) \sqrt{s} \cos(\theta)], \quad \text{and} \quad y_p = y_c + sf [D/(1 + D) \sqrt{s} \sin(\theta)], \quad (85)$$

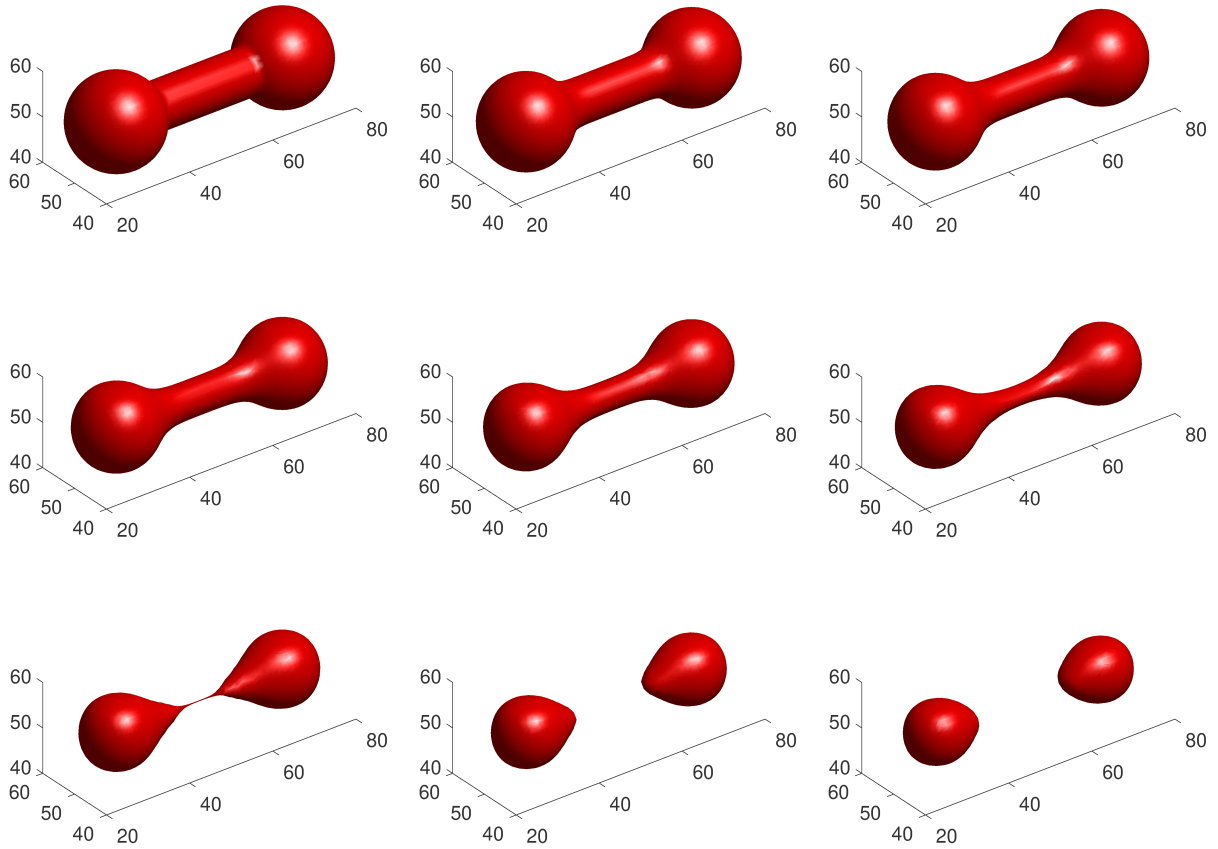


Fig. 6: Evolution of a dumbbell shaped surface under a curvature-driven flow. The images are snapshots in time from left to right, top to bottom where the handle of the dumbbell shrinks faster than the spherical shells due to its high curvature leading to a pinch-off for  $t = 0.0, 2.0, 4.0, 6.0, 8.0, 10.0, 12.0, 14.0, 16.0$ .

where  $\mathbf{x}_c$  is the center location of the domain,  $sf$  the scaling factor for the spiral size and  $D$  the number of spirals. Define a distance function  $d(\mathbf{x}) = \|\mathbf{x} - \mathbf{x}_p\|$  such that the zero level set comes out as

$$\phi(\mathbf{x}, 0) = d(\mathbf{x}) - w \tag{86}$$

where  $w$  is the width of the spirals. The computational domain is a square with side length of a 100 units and a grid size of  $100 \times 100$ . The time step is  $dt = 0.1$  and an  $\alpha = 0.4$ . The wound spiral level curve is centered at  $\mathbf{x}_c = (50, 50)$ ,  $np = 400$ ,  $D = 2.5$ ,  $a = 3$ ,  $sf = 50$ . The code is run for 3000 iterations. Figure 5 shows the progression of the front evolving under the curvature-driven flow for  $t = 0.0, 37.5, 75.0, 112.5, 150.0, 187.5, 225.0, 262.5, 300.0$ . The wound spiral collapses to a circle under this motion where the region of positive curvature (spiral ends) collapse faster than the elongated regions.

### 5.2.3. Dumbbell

The previous examples presented level curves in  $2D$ , we extend our formulation to show that the method is also flexible in  $3D$  where we examine the curvature-driven motion of a dumbbell-shaped level surface. The level surface

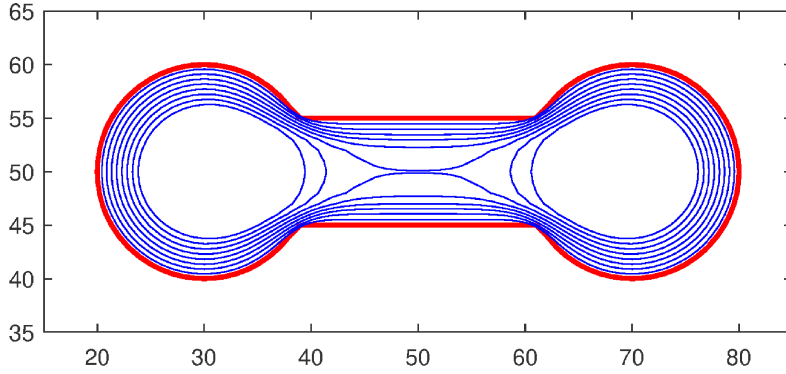


Fig. 7: A 2D slice in the middle of the dumbbell at  $z = 50$  for the zero level set contour evolving under curvature driven motion for the time snapshots mentioned in figure 6.

is initialized by taking advantage of the simplicity of Boolean functions in the level set methodology, where we take the union of two spheres and a cylinder such as

$$\begin{aligned}
 \phi_{left}(\mathbf{x}) &= \sqrt{(x - x_c + o)^2 + (y - y_c)^2 + (z - z_c)^2} - r, \\
 \phi_{right}(\mathbf{x}) &= \sqrt{(x - x_c - o)^2 + (y - y_c)^2 + (z - z_c)^2} - r, \\
 \phi_{center}(\mathbf{x}) &= \max \left[ (|x - x_c| - o), \left( \sqrt{(y - y_c)^2 + (z - z_c)^2} - w \right) \right], \\
 \phi(\mathbf{x}, 0) &= \min[\phi_{left}, \phi_{right}, \phi_{center}],
 \end{aligned} \tag{87}$$

where  $\mathbf{x}_c$  are the domain center coordinates,  $o$  is the distance between the center of the spherical shells and the center of the cylinder,  $r$  the radius of the spherical shells and  $w$  the radius of the center cylinder. Figure 6 demonstrates the ability of the level set methodology to handle pinching, merging and separation of surfaces without any special mathematical or algorithmic “surgery”. The initial dumbbell level set evolves under the motion of mean curvature, the handle shrinks faster due to its higher curvature than the spherical shells on both ends. This leads to a pinch-off at the center where the implicit surface separates into two separate tear drop surfaces that are also shrinking due to curvature. The computational domain is a cube with side length of a 100 units and a grid size of  $100 \times 100 \times 100$ . The time step is  $dt = 0.1$  and an  $\alpha = 0.4$ . The dumbbell level surface is centered at  $\mathbf{x}_c = (50, 50, 50)$ ,  $r = 10$ ,  $w = 5$ ,  $o = 20$ . The case is run for 160 iterations. Figure 6 shows the progression of the front evolving under the curvature-driven flow for  $t = 0.0, 2.0, 4.0, 6.0, 8.0, 10.0, 12.0, 14.0, 16.0$ . Figure 7 shows a cut slice at  $z = 50$  where the evolution of the dumbbell leading up to pinching is more clear.

### 5.3. Motion in the normal direction

Consider a motion in the normal direction where the interface evolves under an internally generated velocity field. The velocity field is defined by  $\mathbf{u} = a\mathbf{N}$  where  $a$  is a constant that can be of either positive or negative. The equations

motion for the level set equation is given by:

$$\frac{\partial \phi}{\partial t} + a\mathbf{N} \cdot \nabla \phi = 0, \tag{88}$$

which can be rewritten as

$$\frac{\partial \phi}{\partial t} + v_n |\nabla \phi| = 0, \tag{89}$$

where  $v_n = a$  is the constant velocity in the normal direction. This motion can also be represented as a case of energy minimization. Express the energy functional in terms of a volume enclosed by the surface  $\phi < 0$  such that

$$\mathcal{E}_{ext}(\phi) = v_n \int_{\Omega} H(-\phi) \, d\mathbf{x}. \tag{90}$$

Taking the Fréchet derivative of  $\mathcal{E}$  with an  $L^2$  norm gives the following

$$\frac{\partial \mathcal{E}_{ext}}{\partial \phi} = -v_n \delta(-\phi) = -v_n \delta(\phi). \tag{91}$$

A similar argument to section 5.2 can be made. The Dirac delta functional singles out the zero level set. In order to obtain motion in the normal direction, all the level sets should minimize their values such that the volume enclosed under each respective level curve  $V_{\beta}(\phi) = H(-\phi - \beta)$  tends to zero. The definition of the energy functional becomes:

$$\mathcal{E}_{ext}(\phi) = -v_n \int_{\beta} \int_{\Omega} H(-\phi + \beta) \, d\mathbf{x} \, d\beta \tag{92}$$

Therefore by definition,

$$\lim_{\epsilon \rightarrow 0} \frac{1}{\epsilon} [\mathcal{E}_{ext}(\phi + \epsilon \chi) - \mathcal{E}_{ext}(\phi)] = \left\langle \frac{\partial \mathcal{E}_{ext}}{\partial \phi}, \chi \right\rangle_{\phi} = -v_n \int_{\beta} \int_{\Omega} \delta(-\phi + \beta) |\nabla \phi| \frac{\chi}{|\nabla \phi|} \, d\mathbf{x} \, d\beta, \tag{93}$$

and

$$\int_{\beta} \int_{\Omega} \delta(-\phi + \beta) |\nabla \phi| \frac{\chi}{|\nabla \phi|} \, d\mathbf{x} \, d\beta = \int_{\Omega} |\nabla \phi| \frac{\chi}{|\nabla \phi|} \, d\mathbf{x}. \tag{94}$$

Now we have

$$\frac{\partial \mathcal{E}_{ext}}{\partial \phi} = -v_n |\nabla \phi| \tag{95}$$

in the level set norm. The evolution equation becomes

$$\frac{\partial \phi}{\partial t} = \alpha \nabla \cdot (d_p(|\nabla \phi|) \nabla \phi) + v_n |\nabla \phi|. \tag{96}$$

The above equation leads to the traditional motion in the normal direction. We validate this type of motion for  $v_n = -1$  and  $v_n = 1$ , where the latter describes the motion by which all the level curves maximize the volume they enclose. Given the above, we compare the effect of reinitialization using DRLSE, traditional reinitialization and no reinitialization.

### 5.3.1. Circle with $v_n = -1$

Consider a level curve given by a circle given by the following implicit equation:

$$\phi(\mathbf{x}, 0) = \|\mathbf{x} - \mathbf{x}_c\| - r. \tag{97}$$

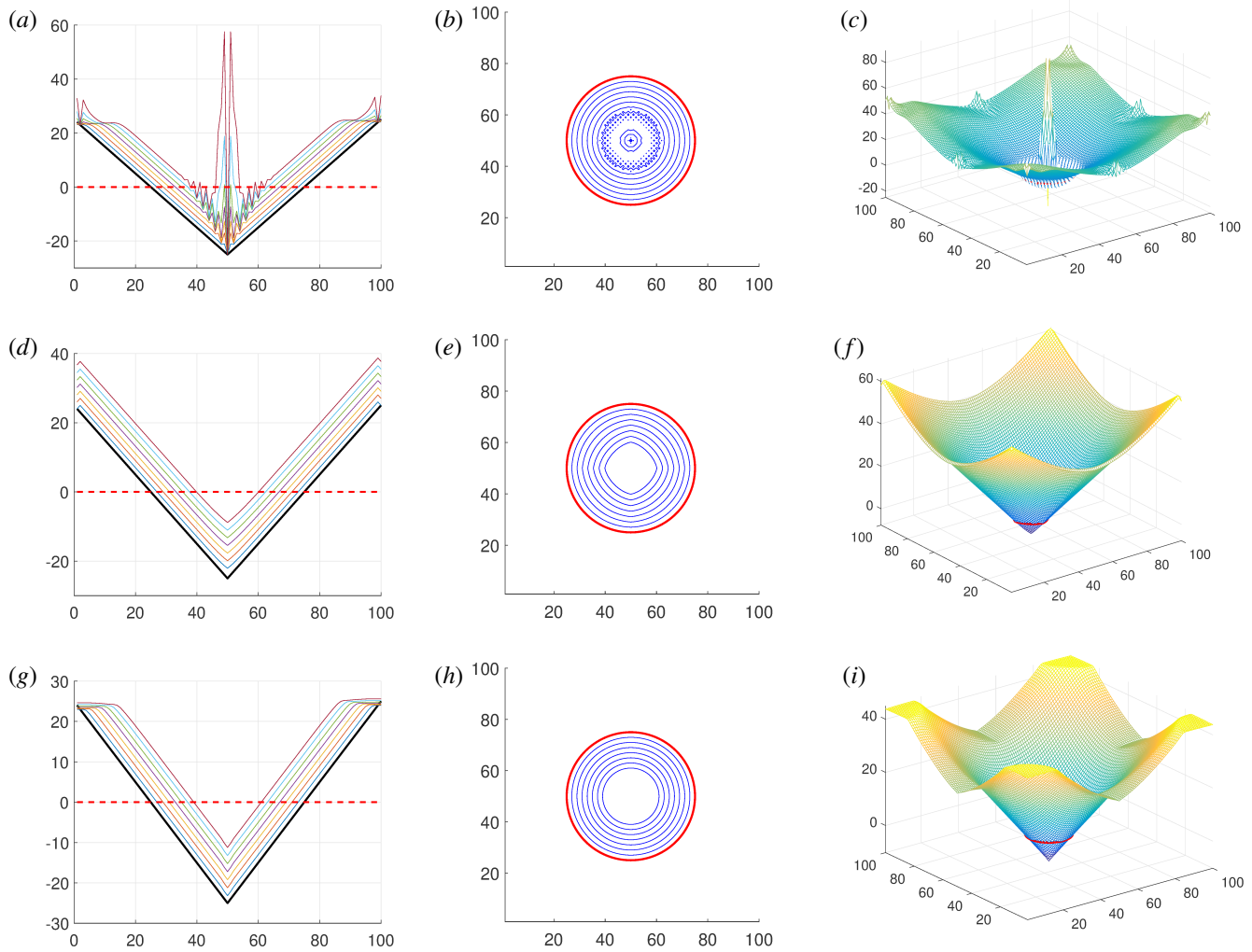


Fig. 8: A comparison of the inward motion in the normal direction of a circle for the level set methodology without reinitialization, traditional reinitialization and DRLSE from top to bottom respectively. Left column is a cut plane at  $y = 50$  for the evolution of the contour over time. The solid thick black line is the initial state, the colored lines are the subsequent time-steps and the red dashed line is the zero level set crossing. The center column is the evolution of the zero level set curves with time, solid red line is the initial condition and the solid blue lines represent the subsequent time-steps. The right most column shows the evolution of the level set surface with the solid red line highlighting the zero level set crossing.

The domain given is a square of size  $100 \times 100$  units of length where  $\mathbf{x}_c = (50, 50)$  and  $r = 25$ . Figure 8 shows the evolution of a contracting circle under a constant velocity  $v_n = -1$  which is a result of minimizing the volume enclosed by  $\phi < 0$ . We solve the equation given by  $\phi_t = |\nabla\phi|$  using DRLSE which is posed as an evolution under a reaction-diffusion equation. For the traditional level set, the equation solved keeps the velocity term on the left hand side  $\phi_t - |\nabla\phi| = 0$  and by uses an ENO scheme for the advection where the level set is reinitialized after each time step.

The top row in figure 8 shows the results from the DRLSE case, middle row for the traditional level set with reinitialization, and the bottom row for traditional level set without reinitialization. The left column (figures 8a,d and g) shows a cut plot in the plane of  $y = 50$ , the solid thick black line is the initial level set location, the subsequent colored lines are the time evolved level sets. The dashed red line indicates the zero level set crossing. The center column (figures 8b,e and h) is a contour plot of the zero level set crossing shown in the thick solid red line, expanding zero level sets over time are shown in the solid blue line. The right column (figures 8c,f and i) shows the final level set function. The first striking feature of not reinitialization the level set is the ringing observed in figure 8(a). This is well known issue; the level curves are no longer signed distance functions as they tend to drift away from their initialized value. The errors accumulate leading each level set curve to intersect and develop noisy features and steep gradients that further corrupt the numerical approximation of  $|\nabla\phi|$ . The advection equation becomes stable once the level set function is re-initialized. The regions where the level set pile up on each other (e.g. near the center of the domain where a kink exists), noisy features develop. This is also evident in figure 8(b) where we clearly observe the unstable level set contours near the center of the domain. In the regions where the level sets separate from each other (domain boundaries), we get the flattening of  $\phi$  as shown in figure 8(a) in the region furthest from the kink. The steepening and flattening effect increase numerical errors as shown in figure 8(c) where numerical errors are the largest in the center. Thus in order to reduce these errors, one has to reset the location of the isocontours of each level curve via reinitialization. Figures 8(d), (e) and (f) show the results of the traditional level set advection with reinitialization. The level set functions are well behaved, figure 8(d) shows the level set moving upwards while maintaining the kink at  $x_c$  with a slight rounding of the edges. The signed distance function is maintained. Figure 8(e) shows the isocontours as the level set moving inwards, note the loss of symmetry in the regions where the normals have either of their component equal to zero. Higher order schemes, finer grids and lower time-steps can correct for those asymmetries. Figures 8(g), (h) and (i) show the results for the DRLSE. Note the level set curve as it shifts upwards in figure 8(g), the kink is maintained at  $x_c$  without any rounding in the corner. The far away field has level sets piling up but it has no effect on the solution since the level set are moving away from the boundaries and towards the center of the circle. Accuracy is maintained as it nears the center, the level curves maintain their circular shape as they advect inwards. Figures 8(f) and (i) show differences in the far away region where the lobes are less uniform but is inconsequential to the final solution. Note that a similar test case was done using  $v_n = 1$  for the circular shape (not shown here); similar behavior was observed.

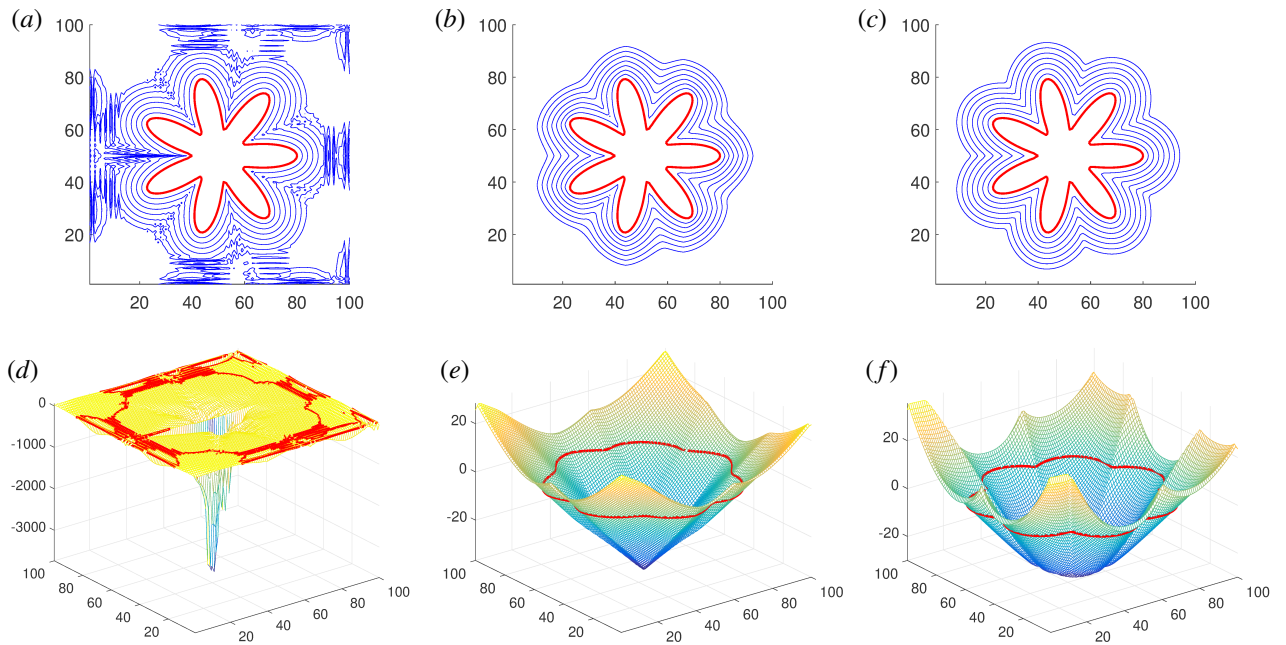


Fig. 9: A comparison of the outward motion in the normal direction of a star-shaped contour for the level set methodology without reinitialization, traditional reinitialization and DRLSE from top to bottom respectively. Top row is the evolution of the zero level set curves with time, solid red line is the initial condition and the solid blue lines represent the subsequent time-steps. Bottom shows the evolution of the level set surface with the solid red line highlighting the zero level set crossing.

### 5.3.2. Seven pointed star with $v_n = 1$

Consider the same implicit function described in section 4.1.1. Figure 9 shows the behavior of a more complicated shape for the case of the outward motion in the normal direction. Qualitatively we get the same trends observed for the circular shape. This makes sure that even more complicated shapes are handled effectively given our numerical scheme. Figure 9(a) shows the ringing being generated in the far field as the zero level set curve advects away from the initial star. Figure 9(b) is well behaved with reinitialization but still loses its symmetrical shapes around the star lobes. The curvature diffuses at a faster rate leading to an early flattening of the curve. Figure 9(c) shows a symmetrical outgrowth of the seven pointed star. As mentioned in previous sections, figures 9(d), (e) and (f) are the final level set surface showing the large numerical errors for the no reinitialization case, and a well behaved final solution for the traditional level set and DRLSE. Similar to the conclusions made above, the flattening of the level set at  $x_c$  is inconsequential to the final solution since the zero level curve is moving away from it.

### 5.4. Energy Minimization

We take the LS formulation of the Gibbs free energy model presented in §3.1 and solve the governing equations using the variational formulation presented in §4. The governing evolution equations are a combination of curvature driven flow with motion in the normal direction. Longitudinal grooves are used first because of the well-defined corners. This causes the interface to pin at the edges and allows for the comparison to Young-Laplace equation. Then a cosine wavy substrate is simulated to compare to the analytic solution obtained by Carbone and Mangialardi (2005).

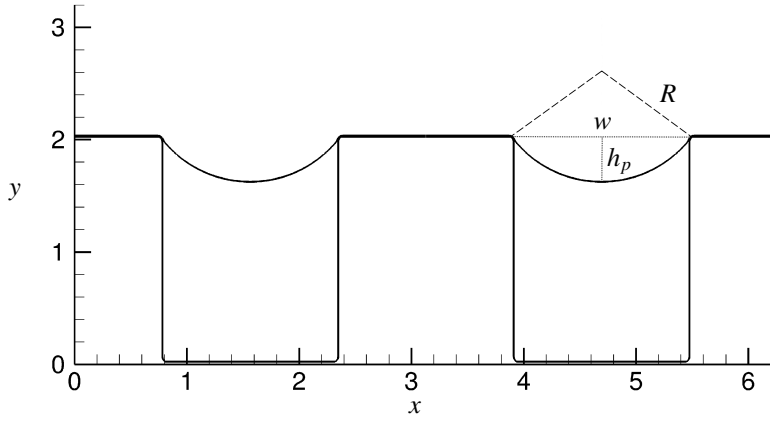


Fig. 10: Equilibrium interface location for a 2D grooved substrate. The thick solid line represents the grooved geometry and the thin solid line the zero level set curve represents the interface. The dashed black line represents the radius of curvature of the meniscus, the small dotted lines denote the width of the groove and the meniscus height from the contact points respectively.

#### 5.4.1. Longitudinal grooves

Consider a rough substrate representing a longitudinal groove, the level set that represents the solid is given by:

$$\psi(\mathbf{x}) = (y - y_c) - \text{sgn} \left[ h, \cos(k_x(x - x_c)) \right], \quad (98)$$

such that  $h = 1$ , the wavelength is  $\pi$  such that  $k_x = 2$  to get multiple grooves. The grooves are shifted by  $\mathbf{x}_c = (0, 1, 0)$  so that the bottom of the surface corresponds to the origin. The domain extents are  $[L_x, L_y, L_z] = [2\pi, 4, 2\pi]$  and domain size  $n_x \times n_y \times n_z = 256 \times 164 \times 1$  for the 2D case. The time-step is taken to be  $\delta t = 10^{-4}$  and  $\alpha = 0.4$ . For an external pressure of  $\Delta p = 1$ , and a non-dimensional  $\tau^- = 1$ , Young-Laplace give a radius of curvature  $R_{analytic} = 1$ . From the current results, the radius of curvature is computed numerically from the contact points and penetration depth  $h_p$  into the groove using  $R_{numerical} = w^2/(8h_p) + h_p/2 = 0.993$  where  $w$  is the groove width. The error is 0.7% showing good agreement with the theoretically predicted results.

#### 5.4.2. Wavy substrate

Consider a wavy substrate using a profile given by:

$$\psi(\mathbf{x}) = (y - y_c) - h \cos(k_x(x - x_c)). \quad (99)$$

The peak to valley height  $h$  of the wavy substrate is taken to be twice the critical height  $h_{cr}$  where  $h_{cr} = -\tan \theta_Y$  (Carbone and Mangialardi, 2005) and  $\theta_Y = 140^\circ$ . The wavelength of the substrate is taken to be  $2\pi$  such that  $k_x = 1$ . The substrate is shifted by  $\mathbf{x}_c = (0, h_{cr})$ . The domain extents are as follows:  $[L_x, L_y, L_z] = [2\pi, 4, 2\pi]$  with a spatial resolution of  $n_x \times n_y \times n_z = 256 \times 164 \times 1$  and a time-step of  $\delta t = 10^{-5}$ . Carbone and Mangialardi (2005) derived an analytical model to predict the interface equilibrium location given an external pressure field. They analyzed the asymptotic behavior of the system and proposed a simple criterion for the minimum  $h_{cr}$  that prevents a Wenzel state. Their solution can predict the pressure value required to overcome the energy barrier to transition from a Cassie state to a Wenzel state. Using our model, we perform a parametric study of different values of pressure and compare the

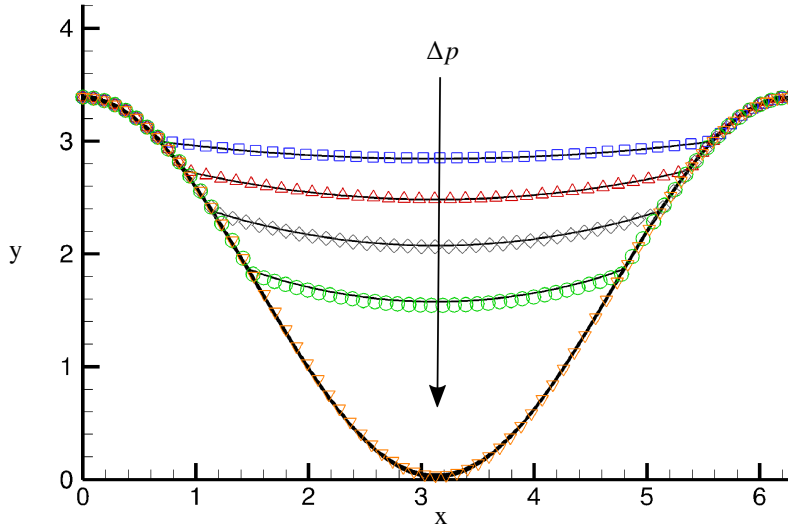


Fig. 11: Equilibrium interface location for a cosine substrate. The solid black lines represent the numerical simulations and the symbols are Carbone's results. The arrow indicates increasing external pressure. Symbols are:  $\Delta p = 0.05$  ( $\square$ ),  $0.1$  ( $\Delta$ ),  $0.15$  ( $\diamond$ ),  $0.2$  ( $\circ$ ),  $0.25$  ( $\nabla$ ).

$\Delta p$	$\bar{y}_{analytic}$	$\bar{y}_{numerical}$	$E(\%)$	$a_{analytic}$	$a_{numerical}$	$E(\%)$	$R_{analytic}$	$R_{numerical}$	$E(\%)$
0.05	2.901	2.906	0.17	0.69	0.71	2.3	19.93	19.316	3.1
0.1	2.57	2.59	0.77	0.91	0.92	1.3	9.93	9.78	1.55
0.15	2.16	2.17	0.55	1.173	1.17	0.085	6.66	6.56	1.54
0.2	1.63	1.66	1.4	1.50	1.49	0.86	4.98	4.944	0.81

Table 1: Comparison between the analytic and numerical values obtained for: the mean LG interface height  $\bar{y}$ , interface contact point  $a$ , and radius of curvature  $R$  for a given external pressure  $\Delta p$ .

resulting interface shape and location with that of the analytic solution. The pressure value that leads to the Wenzel state is obtained using the analytic result for the above conditions comes out to be 0.25. The values of external pressure prescribed are:  $\Delta p = 0.05, 0.1, 0.15, 0.2, 0.26$  where the last value was picked to test if we can predict interface failure. The regularization coefficient for this particular problem was varied to gauge its effect on the interface location. For the first case we use  $\alpha = 0.4$ , for the next two cases we use  $\alpha = 0.8$  and for the last two we use  $\alpha = 0.4$ . We also tested  $\alpha = 0.2$  for the third case (not presented here); overall we did not see an appreciable effect, the error in interface location varied within 1% – 3%. Note that all the selected values of  $\alpha$  satisfy the CFL condition for a given time-step. For all the cases, the simulation is terminated when equilibrium is achieved. This is determined by keeping track of the Gibbs free energy over time where it tends to a steady state. Once the change in  $|(G_{tot}^{n+1} - G_{tot}^n)/G_{tot}^n| < O(10^{-3})$  the simulation is stopped. Figure 11 shows a comparison between our numerical model (solid lines) and the analytic solution (symbols). A good agreement is observed. Note that for the value of  $\Delta p = 0.26$ , the interface fails and lies exactly on top of the cosine substrate. Table 1 shows quantitative results for the mean LG interface height, the triple line contact points and radius of curvature.

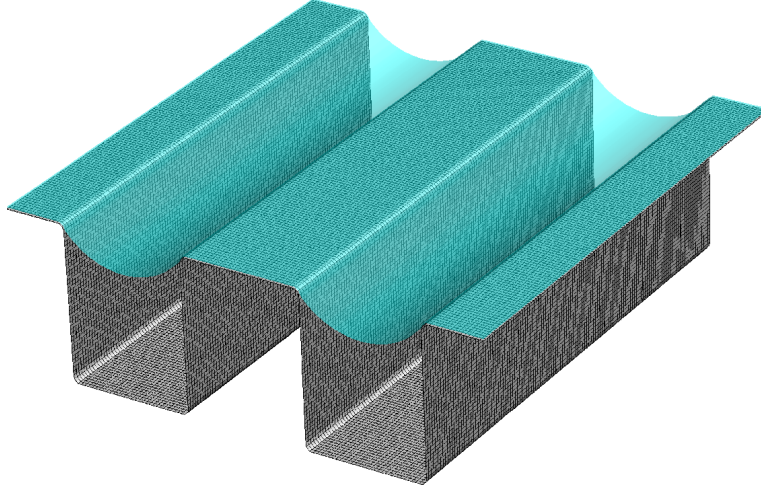


Fig. 12: Equilibrium interface location for a 3D grooved substrate where the gray isosurface represents the rigid substrate and the cyan transparent isosurface of the zero level set represents the interface.

## 6. Numerical Experiments

The numerical results for predicting equilibrium interfacial shapes over a variety of rough surfaces will be discussed. In the earlier section we validated our results against the analytical solution of a cosine substrate obtained by Carbone and Mangialardi (2005) for different loading conditions. We demonstrate the robustness of the algorithm for different geometries such as a 3D wavy substrate, longitudinal grooves, posts, and random roughness.

### 6.1. Longitudinal Grooves

Consider a rough substrate representing a longitudinal groove, the level set that represents the solid is given by:

$$\psi(\mathbf{x}) = (y - y_c) - \text{sgn} \left[ h, \cos(k_x(x - x_c)) \right], \quad (100)$$

such that  $h = 1$ , the wavelength is  $\pi$  such that  $k_x = 2$  to get multiple grooves and  $\text{sgn}$  is the sign function. The grooves are shifted by  $\mathbf{x}_c = (0, 1, 0)$  so that the bottom of the surface corresponds to the origin. The domain extents are  $[L_x, L_y, L_z] = [2\pi, 4, 2\pi]$  and domain size  $n_x \times n_y \times n_z = 128 \times 82 \times 128$  for the 3D case. The time-step is taken to be  $\delta t = 10^{-5}$  and  $\alpha = 0.4$ . For an external pressure of  $\Delta p = 1$ , and a non-dimensional  $\tau^- = 1$ , Young-Laplace give a radius of curvature  $R_{\text{analytic}} = 1$ . From the current results, the radius of curvature is computed numerically similar to the 2D validation case with similar error.

### 6.2. Grooved Posts

In order to represent a post geometry, we make use of the Boolean operations. Consider the level sets that represent the solid:

$$\psi_1(\mathbf{x}) = (y - y_c) - \text{sgn} \left[ h, \cos(k_x(x - x_c)) \right], \quad (101)$$

which represents longitudinal grooves in the  $x - y$  plane extending in the  $z$ -direction, and

$$\psi_2(\mathbf{x}) = (z - z_c) - \text{sgn} \left[ h, \cos(k_z(z - z_c)) \right], \quad (102)$$

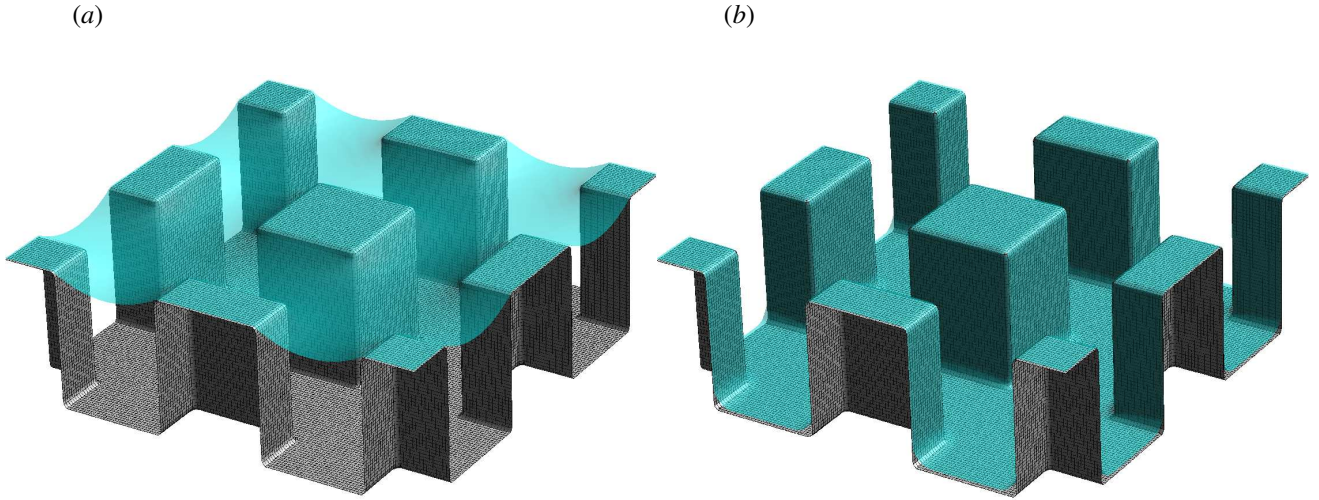


Fig. 13: Equilibrium interface location for post geometries, the gray isosurface represents the rigid substrate and the cyan transparent isosurface of the zero level set represents the interface. (a) Equilibrium shape for  $\Delta p = 0.5$  and (b) interfacial failure at  $\Delta p = 1$ .

the longitudinal grooves in the  $y-z$  plane extending in the  $x$ -direction. Take the intersection  $\psi = \psi_1 \cap \psi_2$  such that

$$\psi(\mathbf{x}) = \max(\psi_1, \psi_2). \quad (103)$$

This gives the post geometry such that  $h = 1$ . The wavelength is  $\pi$  such that we obtain  $k_x = 2$  and  $k_z = 2$ . The domain extents are  $[L_x, L_y, L_z] = [2\pi, 4, 2\pi]$  and domain size  $n_x \times n_y \times n_z = 128 \times 82 \times 128$ . The time-step is  $\delta t = 10^{-5}$  and  $\alpha = 0.4$ . Two different values for external pressure were simulated,  $\Delta p = 0.5$  and  $\Delta p = 1$ . The aim was to demonstrate the capability of predicting failure. At  $\Delta p = 0.5$  the interface goes to equilibrium, when the value for pressure is doubled, the interface is no longer pinned and the interface fails and fills up the grooves. This process of failure is referred to as a depinned recession in (Xiang et al., 2017).

### 6.3. 3D cosine

Consider a three-dimensional wavy substrate that is given by the following level set:

$$\psi(\mathbf{x}) = (y - y_c) - h \cos(k_x(x - x_c)) \cos(k_z(z - z_c)), \quad (104)$$

where the peak to valley height is  $h = 2h_{cr}$  where  $h_{cr} = -\tan \theta_\gamma$  and  $\theta_\gamma = 140^\circ$ . The wavelength in both direction is  $2\pi$  such that  $k_x = 1$  and  $k_z = 1$ . The substrate is shifted by  $\mathbf{x}_c = (0, h, 0)$  so that the valley corresponds to the origin. The domain extents are  $[L_x, L_y, L_z] = [2\pi, 4, 2\pi]$  and domain size  $n_x \times n_y \times n_z = 128 \times 82 \times 128$ . The time-step is  $\delta t = 10^{-5}$  and  $\alpha = 0.4$ . The interface is initialized at  $y = 2.5$  as a binary function, as the interface evolves and moves down towards the solid substrate, the Gibbs energy increases until it reaches steady state when the solution goes to an equilibrium position. The external pressure prescribed is  $\Delta p = 0.2$ , the equilibrium solution is consistent with the two-dimensional case presented in the validation section if a cut plane is taken at  $z = 0$ .

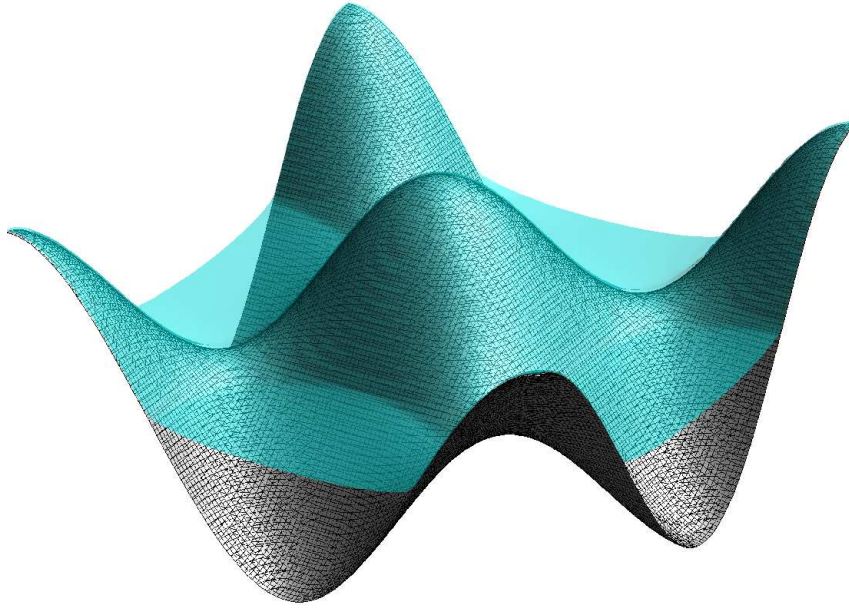


Fig. 14: Equilibrium interface location for a 3D cosine substrate using a loading condition of  $\Delta p = 0.2$ . The gray isosurface represents the rigid substrate and the cyan transparent isosurface of the zero level set represents the interface.

#### 6.4. Random Roughness

A Fractal dimension is used to represent a random rough surface. The geometry is seen as a composition of many elementary waves in the form of  $\cos(\mathbf{k} \cdot \mathbf{x} + \varphi)$ . This is done discretely. Define a range of amplitudes that tapers off based on a certain distribution:

$$h_{mn} = \frac{1}{(m^2 + n^2)^{\beta/2}}, \quad (105)$$

where  $m$  and  $n$  are the wavenumbers and  $\beta$  the spectral exponent. A Gaussian distribution  $g_{mn}$  is used to get a smooth random variation in its amplitudes such that

$$A_{mn} = g_{mn} h_{mn}. \quad (106)$$

The phase angle is also sampled from a Gaussian distribution and is scaled such that it varies between  $-\pi/2$  and  $\pi/2$ :

$$\varphi_{mn} = \frac{\pi}{2} g_{mn}. \quad (107)$$

The rough surface height distribution is then represented by a double sum over the wavenumbers in both spatial directions and is scaled such that the maximum height from peak to valley is scaled to  $2h_{cr}$ :

$$h_f(\mathbf{x}) = \sum_{m,n} A_{mn} \cos(k_{mn} \cdot \mathbf{x} + \varphi_{mn}). \quad (108)$$

Then the level set that represents the solid is given by:

$$\psi(\mathbf{x}) = (y - y_c) - h_f(\mathbf{x}) \quad (109)$$

For this simulation,  $N = 10$  for the spatial frequency resolution,  $\beta = 1.5$  which represents a fairly rugged surface. The domain extents are  $[L_x, L_y, L_z] = [2\pi, 4, 2\pi]$  and domain size  $n_x \times n_y \times n_z = 128 \times 82 \times 128$ . The time-step is  $\delta t = 10^{-5}$

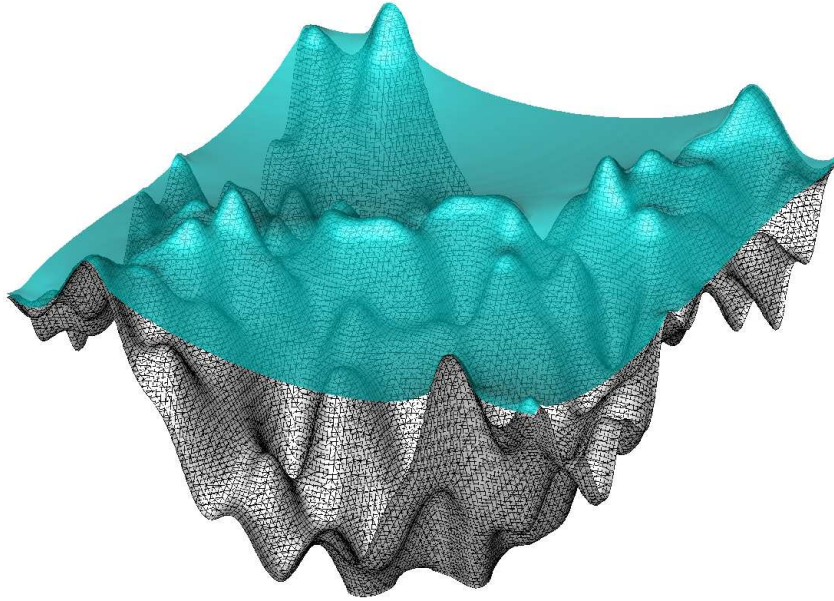


Fig. 15: Equilibrium interface location for a random rough substrate for a loading condition of  $\Delta p = 0.2$ . The gray isosurface represents the rigid substrate and the cyan transparent isosurface of the zero level set represents the interface.

and  $\alpha = 0.4$ . The external pressure is  $\Delta p = 0.2$ , the solver reaches an equilibrium solution and is able to handle rough surfaces that have rapid variations in their structure.

### 6.5. Drop shapes

The drop shape was also investigated where we look at the macroscopic aspect of the equilibrium shape. The bubble is initialized as a binary cuboid over flat surface, longitudinal grooves, posts, and random rough surface using the methods described earlier. The surface parameters are described in the captions of the corresponding figures. All simulations were run using  $\delta t = 10^{-7}$ , with a domain extents of  $[L_x, L_y, L_z] = [1, 1, 1]$  and domain size  $n_x \times n_y \times n_z = 200 \times 200 \times 200$ . Note that here the external pressure was substituted for  $h(\mathbf{x}) \cdot \mathbf{g}$  where  $\mathbf{g}$  is the non-dimensional gravitational constant taken to be unity in the wall-normal direction. When initializing a binary cuboid on rough surfaces, some regions might overlap between the interface and solid LS. Therefore it is best to define  $\phi(\mathbf{x}, 0) = \phi(\mathbf{x}, 0) \cup (-\psi(\mathbf{x}) - \epsilon)$ .

## 7. Summary

A variational level set methodology is developed in the framework of minimizing Gibbs free energy. The level set method avoids reinitialization by using a penalty term that regularizes the distance function. The method is able to reproduce canonical level set evolution cases such as motion in the normal direction and curvature driven flow. The model is general as such it can incorporate an external pressure field with a dissolved gas concentration parameter, and a solid surface that can represent a wide range of geometries. The method is simple to implement, robust and parallel. The surface tension distribution uses a harmonic mean modified to give the desired value of surface tension at

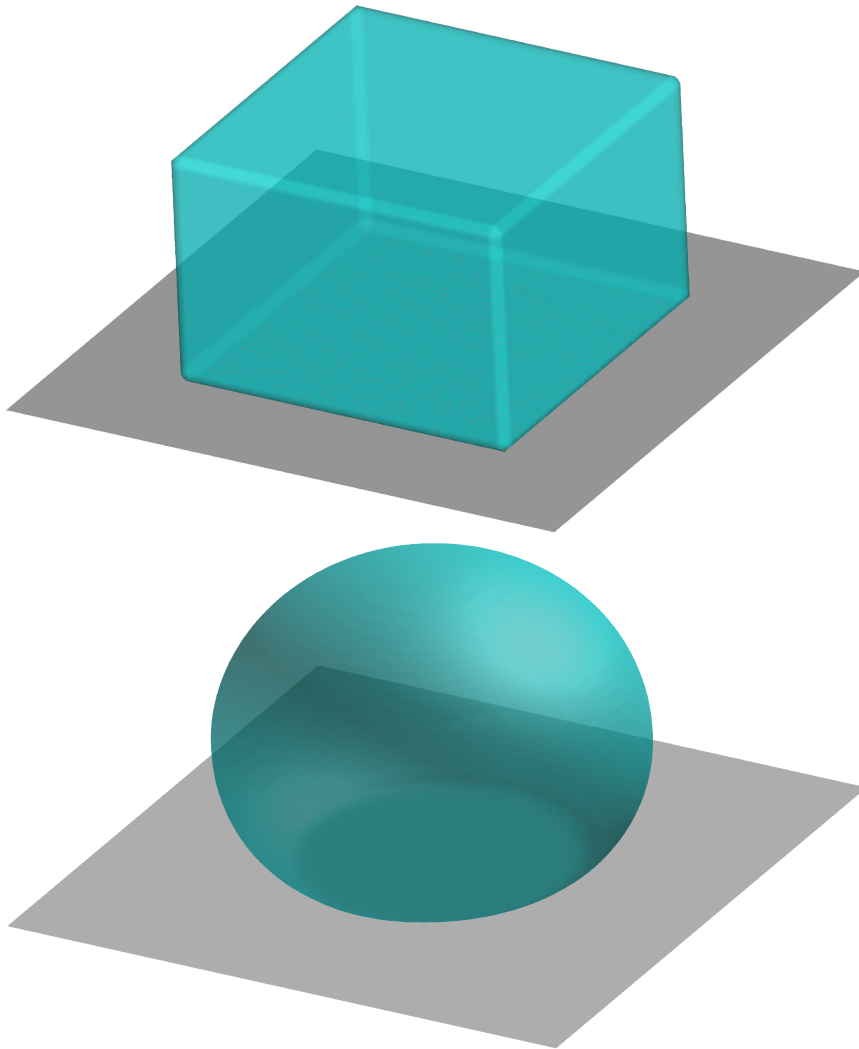


Fig. 16: Drop shape at equilibrium for a flat surface. Top shows the binary cuboid initial condition. Bottom shows the final equilibrium solution for the drop. Surface tension values used are  $\tau^- = 0.6$  and  $\tau^+ = 0.5$  in non-wetted conditions.

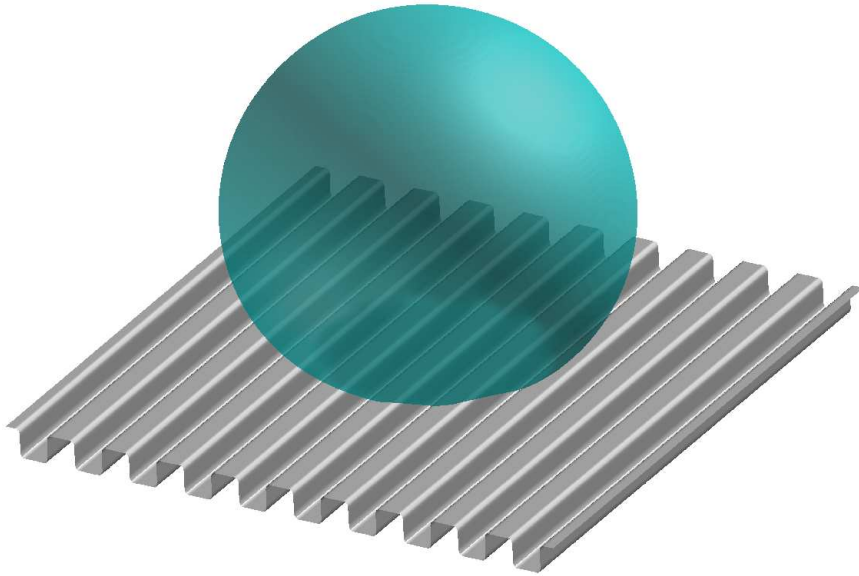


Fig. 17: Drop shape at equilibrium for longitudinal grooves. Here  $h = 0.025$ ,  $k_x = 20\pi$  and  $x_c = (0, 0.15, 0)$ . Figure shows the final equilibrium position for  $\tau^- = 0.6$  and  $\tau^+ = 0.5$  in non-wetted conditions.

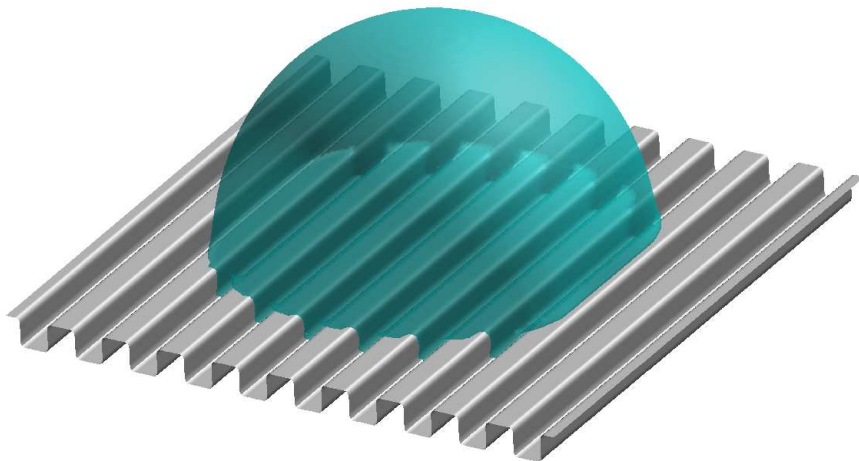


Fig. 18: Drop shape at equilibrium for longitudinal grooves. Here  $h = 0.025$ ,  $k_x = 20\pi$  and  $x_c = (0, 0.15, 0)$ . Figure shows the final equilibrium position for  $\tau^- = 0.6$  and  $\tau^+ = 10^{-3}$  to represent a Wenzel state where the liquid fills the grooves from the initial condition. Note the anisotropy in the drop shape due to wetting.

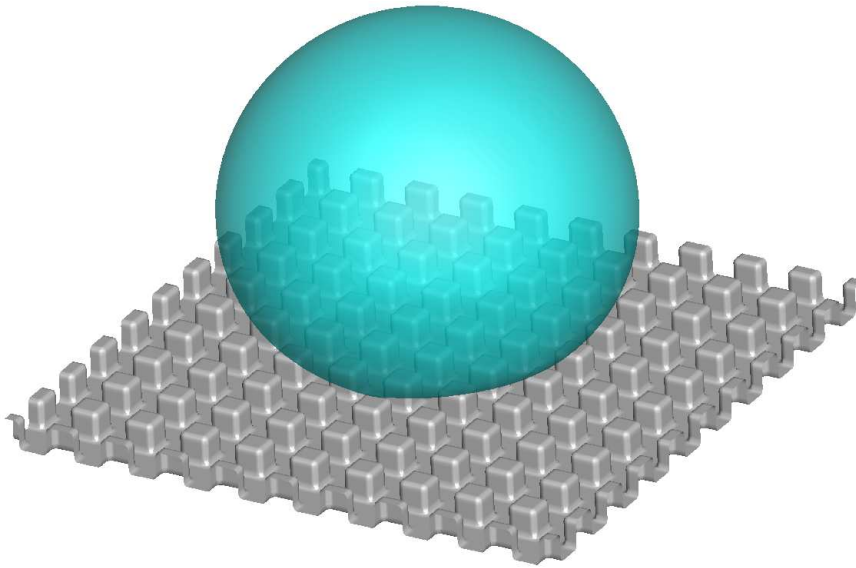


Fig. 19: Drop shape at equilibrium over posts. The geometrical parameters are the same as the longitudinal grooves but is applied in both planes with  $\tau^- = 1$  and  $\tau^+ = 0.833$  in non-wetted conditions.

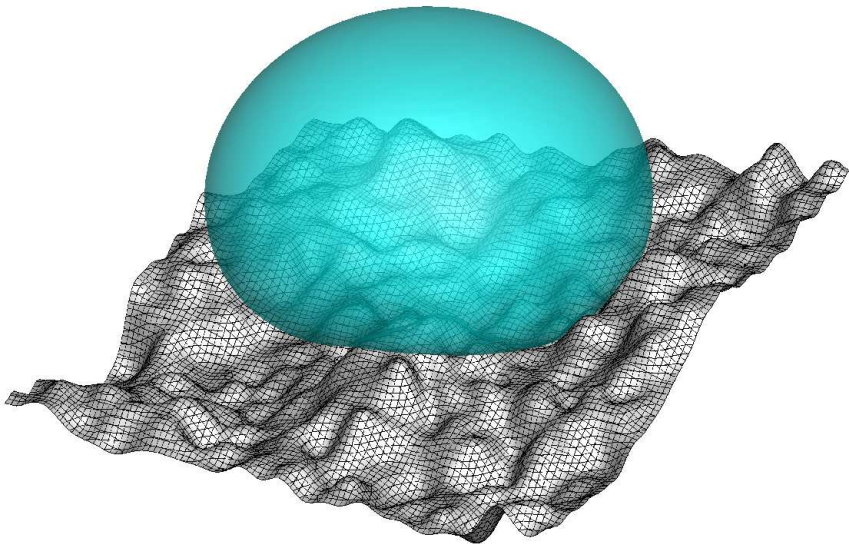


Fig. 20: Drop shape at equilibrium over random rough surface. Spatial frequency resolution  $N = 96$ ,  $\beta = 1.5$  and the mean height  $h_{cr} = 0.15$  with  $\tau^- = 0.6$  and  $\tau^+ = 0.5$  in non-wetted conditions. Note the loss in spherical symmetry in the bubble shape.

the interface location. The solver validated with Young-Laplace and with an analytic solution over a wavy substrate, good agreement is reported. Several geometries were investigated (e.g. longitudinal grooves, posts, a wavy substrate and random roughness using a fractal dimension), the solver is shown to handle complicated geometry. In the context of microscopic problems, gravity effects can be ignored and an external pressure field can be applied to obtain an equilibrium meniscus shape over a wide range of rough surfaces. For macroscopic problems, the effects of gravity can be included. Liquid drops are able to reach an equilibrium shape while conserving its mass. Different surfaces can lead to different equilibrium contact lines where the algorithm is capable of capturing anisotropy in liquid drop shapes.

## Acknowledgement

This work is supported by the United States Office of Naval Research (ONR) under ONR Grants N00014-12-1-0874 and N00014-17-1-2676 with Dr. Ki-Han Kim as technical monitor. The computations were made possible through the Minnesota Supercomputing Institute (MSI) at the University of Minnesota.

## References

- S. Osher, J. A. Sethian, Fronts propagating with curvature-dependent speed: algorithms based on hamilton-jacobi formulations, *Journal of computational physics* 79 (1988) 12–49.
- R. Malladi, J. A. Sethian, B. C. Vemuri, Shape modeling with front propagation: A level set approach (1994).
- J. A. Sethian, *Level set methods and fast marching methods: evolving interfaces in computational geometry, fluid mechanics, computer vision, and materials science*, volume 3, Cambridge university press, 1999.
- S. Osher, R. Fedkiw, *Level set methods and dynamic implicit surfaces*, volume 153, Springer Science & Business Media, 2006.
- D. L. Chopp, Computing minimal surfaces via level set curvature flow, *Journal of Computational Physics* 106 (1993) 77–91.
- M. Sussman, P. Smereka, S. Osher, A level set approach for computing solutions to incompressible two-phase flow, *Journal of Computational physics* 114 (1994) 146–159.
- D. Peng, B. Merriman, S. Osher, H. Zhao, M. Kang, A pde-based fast local level set method, *Journal of computational physics* 155 (1999) 410–438.
- C. Li, C. Xu, C. Gui, M. D. Fox, Distance regularized level set evolution and its application to image segmentation, *IEEE transactions on image processing* 19 (2010) 3243–3254.
- C. E. Brennen, *Cavitation and bubble dynamics*, Cambridge University Press, 2014.
- G. Carbone, L. Mangialardi, Hydrophobic properties of a wavy rough substrate, *The European Physical Journal E* 16 (2005) 67–76.
- F. Bottiglione, G. Carbone, Role of statistical properties of randomly rough surfaces in controlling superhydrophobicity, *Langmuir* 29 (2012) 599–609.
- Y. Chen, B. He, J. Lee, N. A. Patankar, Anisotropy in the wetting of rough surfaces, *Journal of colloid and interface science* 281 (2005) 458–464.
- K. A. Brakke, The surface evolver, *Experimental mathematics* 1 (1992) 141–165.
- H.-K. Zhao, B. Merriman, S. Osher, L. Wang, Capturing the behavior of bubbles and drops using the variational level set approach, *Journal of Computational Physics* 143 (1998) 495–518.
- Y. Xiang, S. Huang, P. Lv, Y. Xue, Q. Su, H. Duan, Ultimate stable underwater superhydrophobic state, *Physical review letters* 119 (2017) 134501.
- V. I. Arnold, *Geometrical methods in the theory of ordinary differential equations*, volume 250, Springer Science & Business Media, 2012.
- C. Li, C. Xu, C. Gui, M. D. Fox, Level set evolution without re-initialization: a new variational formulation, in: *2005 IEEE computer society conference on computer vision and pattern recognition (CVPR'05)*, volume 1, IEEE, 2005, pp. 430–436.
- L. Landau, E. Lifshitz, *Statistical physics, part 1: Volume 5 (course of theoretical physics, volume 5)*, Publisher: Butterworth-Heinemann 3 (1980).
- N. A. Patankar, Hydrophobicity of surfaces with cavities: making hydrophobic substrates from hydrophilic materials?, *Journal of Adhesion Science and Technology* 23 (2009) 413–433.
- T. Frankel, *The geometry of physics: an introduction*, Cambridge university press, 2011.
- A. Giacomello, M. Chinappi, S. Meloni, C. M. Casciola, Metastable wetting on superhydrophobic surfaces: Continuum and atomistic views of the cassie-baxter–wenzel transition, *Physical review letters* 109 (2012) 226102.
- H.-K. Zhao, T. Chan, B. Merriman, S. Osher, A variational level set approach to multiphase motion, *Journal of computational physics* 127 (1996) 179–195.
- S. Esodoglu, P. Smereka, et al., A variational formulation for a level set representation of multiphase flow and area preserving curvature flow, *Communications in Mathematical Sciences* 6 (2008) 125–148.